MONITORING AND TRANSMISSION STRATEGIES FOR LONG-HAUL DIGITAL COHERENT COMMUNICATION SYSTEMS

ZHENHUA DONG

Ph.D

The Hong Kong Polytechnic University

2016

The Hong Kong Polytechnic University

Department of Electrical Engineering

MONITORING AND TRANSMISSION STRATEGIES FOR LONG-HAUL DIGITAL COHERENT COMMUNICATION SYSTEMS

ZHENHUA DONG

A thesis submitted in partial fulfillment of the requirements for the degree of Doctor of Philosophy

Jan 2016

Certificate of Originality

I hereby declare that this thesis is my own work and that, to the best of my knowledge and belief, it reproduces no material previously published or written, nor material that has been accepted for the award of any other degree or diploma, except where due acknowledgement has been made in the text.

…….. (Signed)

DONG ZHENHUA

…….. (Name of student)

Abstract

Over the last decade, fiber-optic communications have evolved from early non-coherent systems to digital coherent systems in order to comply with the exponential growth of bandwidth demand. Advanced optical modulation formats offering high spectral efficiencies have been successfully employed in conjunction with coherent receivers and digital signal processing (DSP). Additionally, complex network architectures utilizing reconfigurable optical add-drop multiplexers (ROADMs), flexible grid, modulation format and bandwidth have been incorporated in order to promote dynamicity, flexibility and better utilization of available transmission capacity. The fundamental technology shift brought about by digital coherent systems also impacted the roles, functionalities and research direction of optical performance monitoring (OPM) and long-haul transmission strategies: 1) Since all the linear impairments such as chromatic dispersion (CD) and polarization-mode dispersion (PMD) can be estimated and fully compensated by numerous DSP algorithms in the digital coherent receiver, system performance is largely determined by the optical-signal-to-noise ratio (OSNR) and hence OSNR monitoring is most vital for long-haul coherent communication systems. 2) Because of Kerr nonlinearities, current fiber-optic transmission technologies designed for linear channels will not be capable of meeting the customer bandwidth demand even equipped with nonlinear compensation techniques such as digital back propagation (DBP). New transmission strategies fundamentally compatible with fiber nonlinearity is expected in the next few years. Therefore, this thesis will focus on the development of OSNR monitoring techniques and nonlinearity-compatible transmission strategies for long-haul digital coherent systems.

In particular, a nonlinearity-insensitive OSNR monitoring technique is proposed as most fiber-optic systems are operating in the weakly nonlinear regime where nonlinear distortions are indistinguishable from ASE noise and thus traditional OSNR monitoring techniques cannot work accurately in such circumstance. It characterize fiber nonlinearity induced amplitude noise correlation among neighboring symbols as a quantitative measure of nonlinear distortions to the signal. By incorporating/calibrating such amplitude noise correlations into an error vector magnitude (EVM)-based OSNR estimator, nonlinearity-insensitive OSNR monitoring can be achieved. Experimental as well as simulation results demonstrate an accurate OSNR monitoring for both 112 Gb/s polarization-

multiplexed (PM)-quadrature phase-shift keying (QPSK) systems and 224 Gb/s PM-16-Quadrature amplitude modulation (QAM) systems where the launched power can go up to 4 dBm.

In addition, OSNR monitoring is still needed ubiquitously across the network including intermediate nodes. However, using full digital coherent receivers with symbol-rate bandwidth is simply too costly and impractical for this purpose. A low-cost and filtering-effect-insensitive OSNR monitor for distributed monitoring of optical networks is proposed. It utilizes reduced-complexity coherent receptions, electrical filtering and radio frequency (RF) power measurements. By measuring the RF power of three different frequency components of the coherently received baseband signals, the proposed technique is also insensitive to spectral narrowing by wavelength selective switches (WSSs). We experimentally demonstrate accurate (<0.7 dB error) OSNR monitoring for various modulation formats and transmission distances, hence different number of WSSs. We also study the robustness of the proposed technique to the fiber nonlinearity, laser effects in a five-channel wavelength-division-multiplexing (WDM) system at 50-GHz spacing and other practical considerations.

Finally, nonlinear frequency division multiplexing (NFDM), a new transmission strategy that incorporates soliton theory with communication theory and fundamentally compatible with fiber nonlinearity is proposed and experimentally verified for the first time. It is based on the framework of nonlinear Fourier transform (NFT) and resembles the commonly-known orthogonal frequency division multiplexing (OFDM) philosophy in that independent information streams are encoded in parallel sub-carriers (eigenvalues) that are analytically shown to be independent of each other upon propagation in an ideal noiseless and lossless fiber channel. In principle, NFDM is also largely immune to XPM effects and thus it can potentially be a fundamental paradigm shift in long-haul WDM optical communications. On-off keying (OOK) modulated NDFM systems are investigated by simultaneous and independent modulation of 3-eigenvalue multi-soliton NFDM signals. The signal set consists of 1-, 2-, 3-solitons as well as their various nonlinear combinations. Error-free transmission over an 1800 km link of standard single-mode fiber (SSMF) with Raman amplification and coherent detection is demonstrated. Extensions to 4-eigenvalue transmissions are also experimentally investigated. Additionally, simulations are performed to study the impact of frequency offset and laser phase noise on such systems and the results show that they are robust to the frequency offset and laser phase noise in a certain range.

Publications Arising From the Thesis

Journal articles

1. Z. Dong, S. Hari, T. Gui, K. Zhong, M. I. Yousefi, C. Lu, P. K. A. Wai, F. R. Kschischang, and A. P. T. Lau, "Nonlinear Frequency Division Multiplexed Transmissions based on NFT," *Photonics Technology Letters*, vol. 27, issue 15, pp. 1621-1623 (Aug. 2015).
2. Z. Dong, K. Zhong, X. Zhou, C. Lu, A.P.T. Lau, Y. Lu, and L. Li, "Modulation-format-independent OSNR monitoring insensitive to cascaded filtering effects by low-cost coherent receptions and RF power measurements," *Optics Express*, vol 23,issue 12, pp. 15971-15982 (2015).
3. Z. Dong, F. N. Khan, C. Lu and A.P.T. Lau, "Optical Performance Monitoring: A Review of Current and Future Technologies," *Journal of Lightwave Technology*, vol. 33, issue 24, pp. (Dec. 2015).
4. Z. Dong, A.P.T. Lau, and C. Lu, "OSNR monitoring for QPSK and 16-QAM systems in presence of fiber nonlinearities for digital coherent receivers", *Optics Express*, vol. 20, issue 17, pp. 19520-19534(2012).

Conference articles

5. Z. Dong, Q. Sui, A. P. T. Lau, K. Zhong, L. Li, Z. Li, and C. Lu, "Optical Performance Monitoring in DSP-based Coherent Optical Systems," in *Proc. OFC 2015*, Los Angeles, Mar. 2015, paper W4D1(invited).
6. Z. Dong, T. Gui, C. Lu, and A. P. T. Lau, "Impact of Frequency Offset and Laser Phase Noise on Nonlinear Frequency Division Multiplexed Systems via the Nonlinear Fourier Transform," in *Proc. Communications and Photonics Conference (ACP)*, 2015, paper ASu3F. 2.
7. Z. Dong, A.P.T. Lau, and C. Lu, "OSNR Monitoring for PM-QPSK Systems in Presence of Fiber Nonlinearities for Digital Coherent Receivers," in *Proc. Optoelectronic Communication Conference (OECC)*, 2012, paper 6B3-3.

Acknowledgments

I am deeply indebted to my supervisor Dr. Alan Pak Tao Lau, for his guidance, ongoing support, patients and sharing of valuable insights.

Also I would like to thank Prof. Lu Chao, from whom I learnt the attitude of research and the way of thinking.

Many thanks to all the other members of Photonics Research Centre, for their help and insightful discussion.

I would also like to acknowledge the support of Hong Kong Government General Research Fund under project number PolyU 152079/14E.

Finally, I can never thank enough my beloved parents for their unwavering love, best wishes and encouragement.

Table of Contents

List of Abbreviations

ACF	Autocorrelation function
ADC	Analogue-digital converter
AOM	Acousto-optic modulator
ASE	Amplified spontaneous emission
AWGN	Additive white Gaussian noise
BPF	Band- pass filter
CD	Chromatic dispersion
CPE	Carrier phase estimation
CPU	Control and process unit
CMA	Constant modulus algorithm
CMMA	Cascaded multi-modulus algorithm
DBP	Digital back propagation
DCF	Dispersion compensating fiber
DGD	Differential group delay
DSP	Digital signal processing
ECL	External cavity laser
EDFA	Erbium doped fiber amplifier
FIR	Finite impulse response
FO	Frequency offset
EVM	Error vector magnitude
FLL	Frequency-locked loop
FWM	Four-wave mixing
GVD	Group velocity dispersion
HD-FEC	Hard-decision forward error correction
IFWM	Intra-channel four-wave mixing

IMDD	Intensity-modulation and direct detection
INFT	Inverse nonlinear Fourier transform
ISI	Inter-symbol-interference
LO	Local oscillator
MC-DBP	multi-channel digital back-propagation
NFT	Nonlinear Fourier transform
NFDM	Nonlinear frequency division multiplexing
NRZ	Non-return-to-zero
ODI	Optical delay interferometer
OFDM	Orthogonal frequency-division multiplexing
OOK	On-off-keying
OPM	Optical performance monitoring
OSA	Optical spectrum analyzer
OSNR	Optical signal-to-noise ratio
PBC	Polarization beam combiner
PBS	Polarization beam splitter
PRBS	Pseudo random bit sequences
PDL	Polarization dependent loss
PM	Polarization multiplexing
PMD	Polarization mode dispersion
PSD	Power spectral density
PSP	Principal states of polarization
QAM	Quadrature amplitude modulation
QPSK	Quadrature phase-shift keying
RF	Radio frequency
ROADM	Reconfigurable optical add/drop multiplexer
RZ	Return-to zero
SD-FEC	Soft decision-forward error correction

SSMF	Standard single mode fiber
SOP	State of polarization
SPM	Self-phase modulation
WDM	Wavelength division multiplexed
XPM	Cross-phase modulation

Chapter 1

Introduction

Fiber-optic communications have seen tremendous growth over the last decade fueled mainly by the incessant and relentless demand for higher capacities. This insatiable demand is spurred by the Internet traffic growth both in terms of number of users and the bandwidth consumed by each user. In order to comply with this exponential growth of capacity demand, fiber-optic communications using intensity-modulation and direct detection (IMDD) have evolved drastically since their birth in the late 1970s by several key technologies, including erbium-doped fiber amplifiers (EDFA), wavelength division multiplexing (WDM), forward error correction (FEC) and Raman amplification.

Most recently, the advances both in optics and electronics such as integrated 90 degree hybrid and high speed digital to analog converter (DAC) have brought the rebirth of coherent detection to the fiber-optic communications. With the aid of digital signal processing, coherent optical system unlocks more degrees of freedom including phase and polarization of an optical carrier for information encoding that enables the use of more complex modulation formats as well as the compensation of fiber-link impairments, which largely improves the spectrum efficiency and capacity of fiber-optic networks.

Since all the linear impairments such as chromatic dispersion and polarization-mode dispersion can be fully compensated, the accumulated ASE noise and fiber nonlinearity become the limiting factors for coherent systems, which also determine the monitoring and transmission strategies for such systems.

1.1. Impairments in the Fiber-optic Communication Links

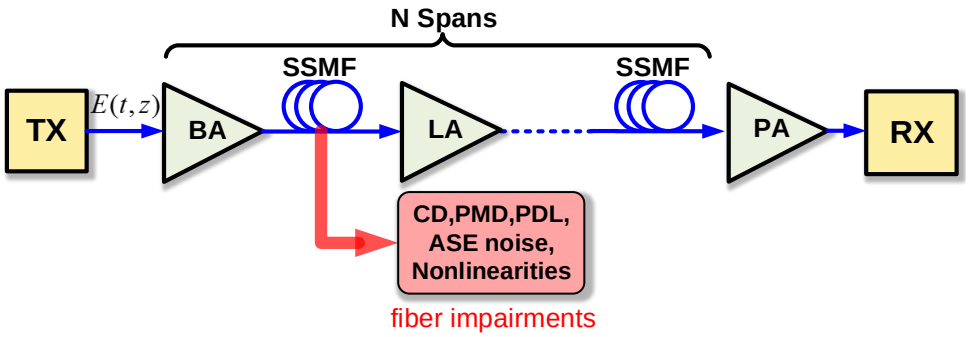

Fig. 1.1 Fiber-optic links and fiber impairments. TX: Transmitter, BA: Boaster EDFA, SSMF: Standard single mode fiber, LA: Inline EDFA, PA: Pre-EDFA, RX: Receiver.

A typical long-haul fiber-optic communication system is shown in

Fig. 1.1, where the optical signal generated by transmitter is firstly amplified by the boaster EDFA and then launched in to the standard single mode fiber. The optical signal is periodically amplified by the inline EDFAs to compensate the fiber loss in each span and is pre-amplified at the end of the links before it goes into the receiver. The propagation of optical field $E(t,z)$ at a given location **z** and time **t** along the fiber is governed by the so-called nonlinear Schrödinger equation (NLSE), which is given by [1]

$$\frac{\partial E(t,z)}{\partial z} + \underbrace{j\frac{\beta_2(\omega)}{2}\frac{\partial^2 E(t,z)}{\partial t^2}}_{\text{dispersion}} - \underbrace{j\gamma\,|E(t,z)|^2\,E(t,z)}_{\text{Kerr nonlinearity}} + \underbrace{\frac{\alpha}{2}E(t,z)}_{\text{attenuation}} = \underbrace{n(t,z)}_{\text{noise}}, \tag{1.1}$$

where α is the attenuation coefficient, $\beta_2(\omega)$ is the group-velocity dispersion (GVD) parameter evaluated at frequency ω, γ is the fiber nonlinear coefficient and *n(t,z)* is the field that represents the ASE noise. This equation accounts for both linear and nonlinear impairments introducing to the optical signals among propagating in fiber links. It will be more closely examined in the following sections.

1.1.1. Linear Impairments

1.1.1.1 Chromatic Dispersion

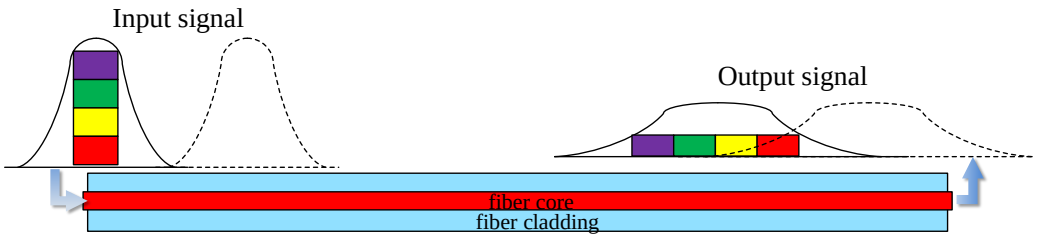

Fig. 1.2 Chromatic dispersion causes broadening and ISI of unchirped pulses

Chromatic dispersion is one of the major linear impairments in a fiber link that is caused by the frequency dependence of the refractive index (material dispersion) and the frequency dependent wave guidance in the fiber core and fiber cladding (waveguide dispersion). Mathematically, CD is defined via the Taylor expansion of the mode-propagation constant β as a function of the angular frequency around the center frequency ω_0,

$$\beta(\omega) = \beta_0 + \beta_1(\omega - \omega_0) + \frac{1}{2}\beta_2(\omega - \omega_0)^2 + \cdots, \tag{1.2}$$

where the zero-order term β_0 describes a common phase shift, the first-order term $\beta_1 = \frac{\partial\beta(\omega)}{\partial\omega}$ is the group delay per unit length and describes an overall time delay without an effect on the pulse shape and the second-order dispersion term $\beta_2 = \frac{\partial^2\beta(\omega)}{\partial\omega^2}$ represents group-velocity dispersion (GVD) that causes pulse broadening.

The relation between β_2 and the more commonly used chromatic dispersion parameter D is

$$D = -\frac{2\pi c\beta_2}{\lambda^2} \tag{1.3}$$

where c is the speed of light in vacuum and D is in units of picoseconds per nanometer and kilometer (ps/(nm km)). As optical signals always has a finite spectral width (bandwidth), dispersion can cause their different frequency components to propagate with different group velocities. Normal dispersion ($\beta_2>0$) leads to a lower group velocity of higher-frequency components, and thus to a positive chirp,

whereas anomalous dispersion ($\beta_2<0$) creates negative chirps. If the transmitted pulses are initially unchirped, dispersion will cause pulse broadening and leads to inter-symbol interferences (ISI) (as shown in Fig. 1.2) that is one of the most common degradations to the system performance. In IMDD systems, for point-to-point links the chromatic dispersion can be compensated by the dispersion compensating fiber (DCF). For high symbol rate systems (exceeding 40 Gbaud), or for flexible routed optical networks, an adaptive dispersion compensator is necessary since the amount of accumulated dispersion varies as the fiber length fluctuations caused by temperature or varies as the changing of routings. For digital coherent systems, since both the amplitude and phase information are recovered, the CD compensation can be performed efficiently in the electrical domain by applying a finite impulse response (FIR) filter with following frequency-domain transfer function [1][2]

$$H(z,\omega)=\exp(-j\beta_2\omega^2 z/2). \tag{1.4}$$

1.1.1.2 Polarization-Mode Dispersion and Polarization-Dependent Loss (PDL)

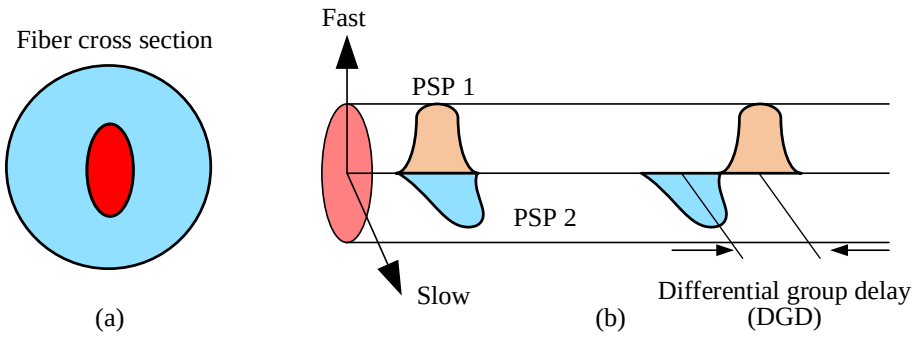

Fig. 1.3 The PMD effect introduced by the asymmetric profile of the optical fiber core. PSP: Principal state of polarization. DGD: Differential group delay.

Polarization-mode dispersion is a kind of modal dispersion due to the random imperfections and asymmetries of the fiber (this property is denominated as “birefringence”) causing different delays for different polarizations that leads to the overlapping of optical pulses and limits the transmission capacity. PMD is usually described in Stokes space, where an input polarization vector S_{in} produce the output vector S_{out} in a frequency dependent manner [3]

$$\frac{d}{d\omega}S_{out}=\Omega\times S_{in}. \tag{1.5}$$

Ω is the Stokes PMD vector that is a function of frequency. The Nth derivative of the PMD vector with respect to angular frequency ω characterizes the Nth order PMD.

The first order PMD describes a phenomenon that the two different principal states of polarization (PSP) of light in a fiber, which normally propagate at the identical speed, propagate at different speeds (as shown in

Fig. 1.3(b)) and the resulting relative delay between them is denoted as differential group delay (DGD). In order to investigate the effect of PMD, a fiber can be approximated by series of many short polarization sections with different constant birefringence and the PMD of k^{th} section is described in Jones space as [3]

$$H_{PMD} = R_{k+1}\begin{bmatrix} e^{-j\omega\Delta\tau/2} & 0 \\ 0 & e^{j\omega\Delta\tau/2} \end{bmatrix} R_k \tag{1.6}$$

where $\Delta\tau$ is the DGD, R_m denote unitary polarization rotation matrices satisfying

$$R_m = \begin{bmatrix} \cos\theta_m e^{-j\varphi_m/2} & \sin\theta_m e^{j\varphi_m/2} \\ -\sin\theta_m e^{-j\varphi_m/2} & \cos\theta_m e^{j\varphi_m/2} \end{bmatrix}, \quad m = 1, 2, 3... \tag{1.7}$$

The random birefringence of fibers can either stem from imperfect fabrications of fiber cores (as shown in

Fig. 1.3(a)), or by the thermal and mechanical stress-induced material birefringence. As the latter stresses generally vary over time, the relative delay between PSPs correspond to a random walk, and thus has a mean $\langle\Delta\tau\rangle$ following the Maxwell distribution

$$f_{\Delta\tau}(x) \sim \frac{32x^2}{\langle\Delta\tau\rangle\pi^2}\exp(-\frac{4x^2}{\langle\Delta\tau\rangle^2\pi}), \tag{1.8}$$

which is proportional to the square root of propagation distance z [3]:

$$\langle\Delta\tau\rangle = D_{\text{PMD}}\sqrt{z} \tag{1.9}$$

where D_{PMD} is the PMD parameter of the fiber, typically measured in $ps/\sqrt{km}$. For those fibers deployed after the year 2000, the PMD parameter has a typical value of about $0.1ps/\sqrt{km}$ [3]. Since the DGD scales with $\sqrt{z}$, the PMD effect is very weak for those fibers for data rate below 10 Gbit/s, even for large distances. However, for those commercially deployed IMDD systems of which data rates

equal to or higher than 40 Gbit/s, the PMD can be a limiting propagation effect. The compensation of PMD effects in IMDD systems is very tricky and expensive since they are random and time-variant. This requires an active component that can monitor the PMD of the links or can respond to feedback over time which limits the deployment of PMD compensators in large scale fiber-optic communication systems [3]. Fortunately, as the evolution of fiber-optic systems to the coherent detection with advanced DSP, PMD will not be a limiting factor since it can be completely compensated by the DSP using constant modulus algorithm (CMA) with multi-taps [2].

Polarization-dependent loss (PDL), denoted as the difference between the maximum and minimum loss in decibels (dB), is a PMD related effect in which two polarizations undergo different extent of loss due to the birefringence of the fiber links. Its mathematical modeling is given by the following matrix

$$H_{PDL} = R^* \begin{pmatrix} 1 & 0 \\ 0 & e^{-PDL} \end{pmatrix} R \tag{1.10}$$

where R is defined in (1.7) and '*' denotes conjugated transpose. PDL varies as the polarization state of the propagating wave changes and is mainly contributed by the imperfections or aging of the inline passive optical components. PDL is not yet the limiting factor for the IMDD systems where signals are modulated on one polarization and it is equivalent to an excess of insertion loss, whereas for coherent systems in which polarization multiplexing (PM) is applied, it may result in uneven BER performance of the two polarizations [3].

1.1.1.3 **Attenuation and Amplified Spontaneous Emission Noise**

The fourth term on the left hand side of (1.1) models the attenuation of light travelling along the fiber links which is mainly due to the material absorption and Rayleigh scattering. In absence of CD and nonlinearity (the second and third term on the LHS of (1.1)), the solution to the equation (1.1) would be

$$|E(t,z)|^2 = |E(t,0)|^2 \, e^{-\alpha z}. \tag{1.11}$$

Equation (1.11) shows that the signal power will attenuates exponentially as distance increases.

The attenuation of fiber links can be compensated by the use of optical amplifiers, for instance

EDFA and Raman amplifier. However, each optical amplifier adds ASE noise and degrades the quality of the signals, normally represented by the OSNR. ASE noise is generated by spontaneous decay of electrons in the upper energy levels to lower energy levels in the atoms of Erbium doped fiber. This results in the emission of photons in a wide frequency range. The power spectral density (PSD) of ASE noise is given by [4]

$$PSD_{ASE} = \eta_{sp} h\nu_0 (G-1) \tag{1.12}$$

where η_{sp} is the spontaneous emission factor, h is the Plank's constant, ν_0 is the signal central frequency and G is the gain of the amplifier. In a fiber transmission link with N_A amplifiers, the OSNR is given by

$$OSNR = \frac{P_{Sig}}{N_A 2 P_{ASE}} \tag{1.13}$$

where P_{Sig} is the total signal power in a given channel bandwidth, P_{ASE} is the ASE noise power defined by

$$P_{ASE} = PSD_{ASE} \cdot B_0 \tag{1.14}$$

where B_0 is the reference noise bandwidth usually defined as 0.1 nm around 1550 nm.

According to the Shannon's theory [5], the channel capacity of a single additive white Gaussian noise (AWGN) channel is given by

$$C = B \log_2 (1 + SNR), \tag{1.15}$$

where SNR is the signal to noise ratio and B is the channel bandwidth in Hz. In an optical fiber channel, since the signal power P_{sig} that can be launched into the fiber is bounded by the Kerr nonlinearity, the accumulation of ASE noise P_{ASE} is one the major impairments that limits the reachable transmission lengths and the channel capacity of an optical channel.

1.1.2. Nonlinear Impairments

Another category of impairments originated from the intensity dependence of the refractive index of the fiber is called Kerr nonlinearity. The refractive index can be written in its simplest form as [1]

$$\tilde{n}(\omega, |E(t,z)|^2) = n_0(\omega) + n_2 |E(t,z)|^2, \tag{1.16}$$

where $n_0(\omega)$ is the linear part of the refractive index and n_2 is the nonlinear part. The intensity dependence of the refractive index leads to two most widely studied nonlinear effects that are self-phase modulation (SPM) and cross-phase modulation (XPM). Self-phase modulation refers to the self-induced phase shift experienced by an optical field during its propagation in optical fibers and can be explained from the third term on the left hand side of (1.1). Since the refraction index is proportional to the local irradiance of the light, the intensity-dependent nonlinear phase shift due to SPM is [1]

$$\phi_{NL} = n_2 k_0 L \left| E(t,z) \right|^2, \tag{1.17}$$

where $k_0=2\pi/\lambda$ and L is the fiber length.

In a same scenario, the phases of the channels can also be shifted due to the intensity variations of the neighboring channels in muti-channel systems and it is referred to as cross phase modulation (XPM). Its origin can be understood by noting that when two optical fields at frequencies ω_1 and ω_2, polarized along the x axis, propagate inside the same fiber, the total electric field E is given by [1]

$$E(t,z) = \frac{1}{2}\hat{x}[E_1(t,z)e^{(-j\omega_1 t)} + E_2(t,z)e^{(-j\omega_2 t)} + \text{c.c.}], \tag{1.18}$$

where the abbreviation c.c. stands for complex conjugate. The nonlinear phase shift for the field at ω_1 is then given by

$$\phi_{NL} = n_2 k_0 L(\left|E_1(t,z)\right|^2 + 2\left|E_2(t,z)\right|^2). \tag{1.19}$$

The second terms on the right-hand side of (1.19) is due to XPM whereas the first term is due to SPM. An important feature of XPM is that, for equally intense optical fields of different wavelengths, the contribution of XPM to the nonlinear phase shift is twice that of SPM. However, the XPM efficiency is reduced due to the dispersive walk-off induced by different group velocities of different channels and XPM only occurs in the time intervals where the propagating pulses are superimposed.

A third nonlinear effect is called four wave mixing (FWM) which describes the generation of new waves at other frequencies by exciting the total electrical field of a WDM signal to the third power [1]. When three frequencies f_i, f_j and f_k interact in a fiber, they give rise to a fourth wavelength

$$f_{ijk} = f_i + f_j - f_k \tag{1.20}$$

which is formed by the scattering of the incident photons, producing the fourth photon. A total number

$$N_{FWM} = \frac{1}{2}\left(N_{WDM}^{3} - N_{WDM}^{2}\right) \tag{1.21}$$

of new mixing products is generated, where N_{WDM} corresponds to the number of WDM channels. In the WDM systems with standard fix channel spacing, the mixing products will fall into the signal bands of the WDM channels and thus introduce distortions to the signals. However, as significant FWM occurs only when the phase match is satisfied, the efficiency of FWM will decrease due to the chromatic dispersion and thus FWM is not considered to be a limiting effect for coherent systems where large accumulated CDs exist in the links and are only compensated at receiver end.

Thanks to the recent advances in coherent optical communication and DSP, the three Kerr nonlinearities, in principal, can be fully compensated using multi-channel digital back-propagation (MC-DBP) with joint detection [6]. However, due to the presence of ASE noise in practical EDFA/Raman assisted systems, the nonlinear interactions between signal, CD and ASE noise make the channel transfer function nondeterministic and noninvertible, which eventually limit the achievable fiber capacity.

1.2. Evolution of Fiber-optic Communication Systems from IMDD Systems to Digital Coherent Systems

Long-haul optical fiber systems always evolve to transmit higher data throughput over longer distance without signal regeneration. Back to the late 1980s, coherent optical fiber communications have already attracted a lot of attention as its high sensitivity that could elongates the unrepeated transmission distance. However, their attractions faded as rapid progress in EDFA and WDM for IMDD systems. Such non-coherent systems use semiconductor lasers for intensity modulation, and the intensity of optical signals transmitted through fibers is detected by a photodiode, which acts as a square-law detector,

$$I_{IMDD} = R\,|E_s(t)|^2 \tag{1.22}$$

where R denotes the responsively of the photo-diode. An eye diagram of intensity modulation signals and the detection scheme are shown in Fig. 1.4,

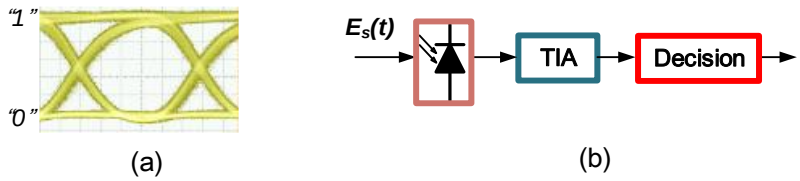

Fig. 1.4 (a) An eye diagram of binary intensity modulation and (b) detection schemes for IMDD system.

In 2005, the successful demonstration of digital carrier-phase estimation in coherent receivers led to the renewal of interests in coherent detection due to the fact that it unlocks the degrees of freedom of phase and polarization of an optical carrier for information encoding [2]. It enables us to employ higher order modulation formats such as PM-QPSK and PM-16QAM to transmit data rates per channel beyond 100Gbit/s. Furthermore, since the phase and polarization information are preserved after detection, electrical post-processing can be realized to compensate the chromatic dispersion and polarization-mode dispersion in the electrical domain [2]. A standard coherent receiver with typical DSP algorithm blocks is shown in Fig. 1.5 (a). The received optical signals $E_s(t)$ firstly interfered with the light from local oscillator in the 2 ×4 90 °hybrid realizing phase and polarization diversity detection.

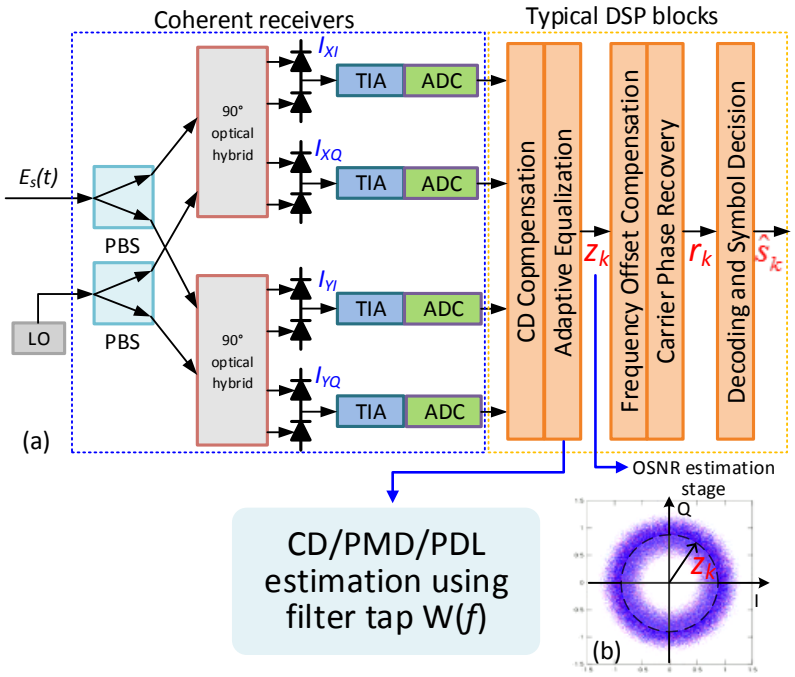

Fig. 1.5 Schematic of a standard coherent optical receiver with typical DSP algorithms for data recovery (a). Adaptive equalizer outputs are used for OSNR monitoring (b). (LO: local oscillator, PBS: polarization-beam splitter, TIA: trans-impedance amplifier, ADC:

After balance detection, the baseband electrical signals are given by

$$\begin{cases} I_{X(Y)I} = R(\left|E_{SX(Y)I} + E_{LO}\right|^2 - \left|E_{SX(Y)I} - E_{LO}\right|^2) = 2R \cdot \mathrm{Re}\left\{E_{SX(Y)I} \cdot E_{LO}\right\} \\ I_{X(Y)Q} = R(\left|E_{SX(Y)Q} + E_{LO}\right|^2 - \left|E_{SX(Y)Q} - E_{LO}\right|^2) = 2R \cdot \mathrm{Im}\left\{E_{SX(Y)Q} \cdot E_{LO}\right\} \end{cases} \quad (1.23)$$

where R is a linear scaling factor and the subscript X(Y) denotes the X or Y polarization tributary of $E_s(t)$. Obviously, unlike the square-law detection of IMDD systems (see (1.22)), coherent detection enables linear detection of the electrical field of transmitted signal $E_s(t)$ and make it possible to design much more complicated transmission scheme and compensate the channel impairments in the electrical domain. After sampling by the ADCs, the signals are then processed by following typical DSP algorithms [2] (as shown in Fig. 1.5 (b)): 1) CD compensation, 2) adaptive equalization for residual CD, PMD, polarization de-multiplexing and timing errors using CMA or pilot-symbol based algorithms, 3) frequency offset compensation, 4) carrier phase estimation and symbol decision followed by decoding (for hard-decision forward error correction (HD-FEC)) or decoding followed by symbol decision (for soft-decision forward error correction (SD-FEC)).

In the last decade, the advance of the digital coherent receiver has enabled the 100-Gbit/s coherent transmission system, which employ QPSK modulation, polarization multiplexing, and phase-diversity homodyne detection assisted with high-speed DSP at a symbol rate of 25 Gbaud, to be developed into commercial networks. A total capacity of up to 8.8 Tbit/s through a single mode fiber was reported in [7] by placing WDM channels at 50-GHz spacing in the whole C+L band. Now worldwide efforts are made to develop commercial available coherent receivers using dual-carrier 16- or 32-QAM that can work at a bit rate of 400 Gbit/s per channel [8][9]. Most recently, Terabit coherent optical transmission using Nyquist shaped PM-64-QAM signal has already been experimentally demonstrated in [10].

1.3. Monitoring Strategies for Digital Coherent Systems

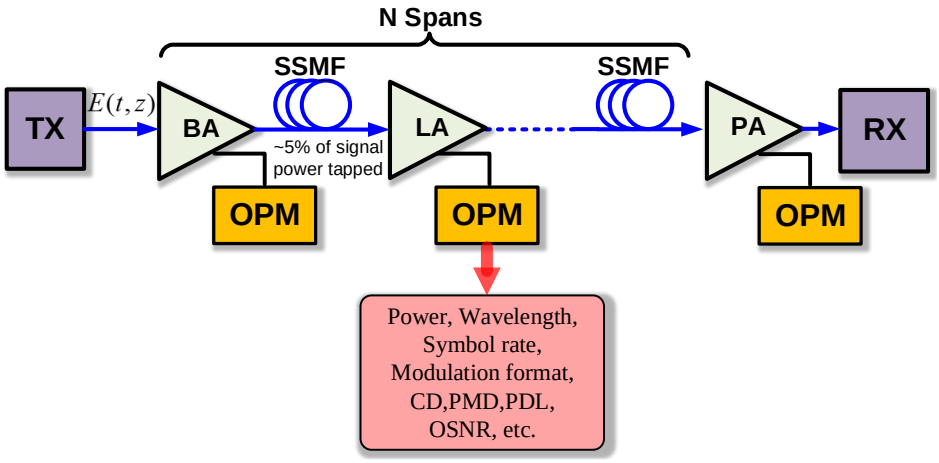

Fig. 1.6 A fiber-optic network equipped with OPM capability to monitor several possible transmission parameters.

Optical performance monitoring is essentially a set of measurements performed on an optical signal to estimate the physical parameters such as signal power, CD, PMD and OSNR of an optical channel that enables the management and maintenance of fiber-optic communication networks. OPM assesses the quality of signal transmission indirectly from the estimates of the optical channel at intermediate nodes of networks or at the receiver side, preferably without disturbing data traffic (as shown in Fig. 1.6).

The capacity of optical communication systems is increasing unremittingly and the architectures of optical networks are continuously becoming more complex, transparent and dynamic in nature. These high-capacity fiber-optic networks are vulnerable to several transmission impairments which can alter over time due to dynamic nature of these networks [11]. On the other hand, in future reconfigurable and dynamic optical networks, flexible payload switching, wavelength allocation and potentially impairment-aware routing would not be possible without the information of link. Therefore, it is imperative to incorporate effective monitoring mechanisms across the whole fiber-optic network which can provide precise and real-time information about the health of each individual DWDM channel.

Over the past decades, a plethora of OPM techniques for IMDD fiber-optic networks have been proposed. A general classification of these techniques is shown in Fig. 1.7. The existing OPM approaches can be classified into time domain, frequency domain and polarization domain techniques

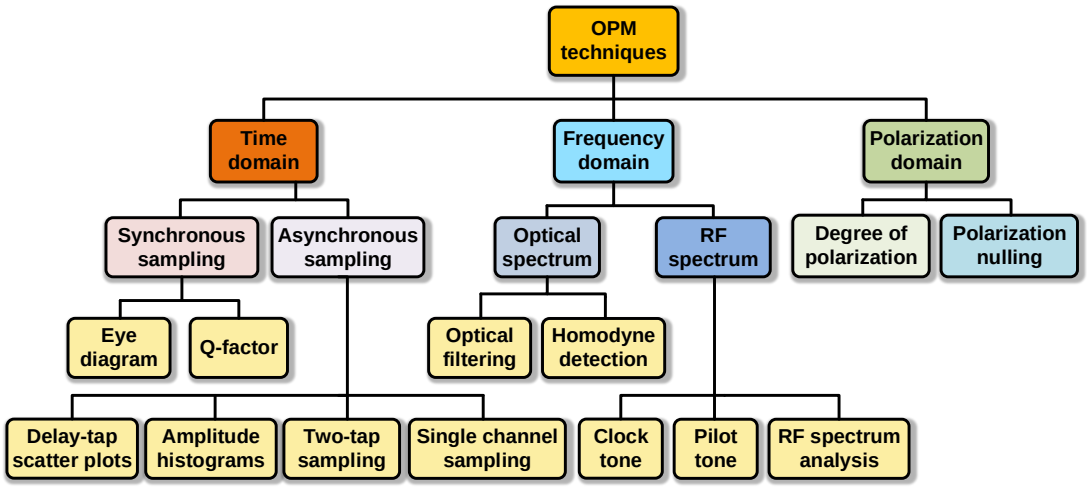

Fig. 1.7. Classification of existing OPM techniques for direct detection systems.

according to whether the monitoring information is extracted from the signal waveform, signal spectrum or the signal polarization, respectively.

However, as the fiber-optic communication systems evolve from IMDD systems to digital coherent systems, the fundamental technology shift brought about by digital coherent communications also impacted the roles, functionalities and research direction of OPM in optical networks. At a first glance, many commonly used OPM techniques proposed for IMDD systems, such as interpolation based out-band OSNR monitoring or polarization nulling based in-band OSNR monitoring techniques [12][13], are no longer suitable for coherent detection with very tight channel spacing, Nyquist pulse shaping and polarization multiplexing. As a result, new OPM strategies are needed for digital coherent systems,

1) Since all the linear impairments such as CD and PMD can be monitored and fully compensated by linear filters at the digital coherent receiver [14], transmission performance is largely determined by the OSNR and hence OSNR monitoring is especially vital for coherent systems. Research efforts will focus on higher performance and/or lower complexity OSNR monitoring algorithms that can be realized by DSP as a by-product of the digital coherent receiver.

2) Most currently deployed fiber-optic systems are operating in the weakly nonlinear regime where nonlinear distortions are typically treated as noise and are indistinguishable from amplifier noise. As a result, traditional OSNR monitoring techniques cannot work accurately in such circumstance and nonlinearity-insensitive OSNR monitor is in great demand.

3) OSNR monitoring is still needed ubiquitously across the network including intermediate nodes. However, using full digital coherent receivers with symbol-rate bandwidth is simply too costly and impractical for this purpose. Low-cost monitoring solutions utilizing reduced-complexity and low-speed hardware are still highly desirable.

1.3.1. CD and PMD monitoring

Before the revival of digital coherent systems, several CD and PMD monitoring techniques were proposed such as either utilizing the clock tones present inherently in the spectrum of various modulation formats [17]- [20] or insert pilot tones at different frequencies at the transmitter side [21]-[24]. The clock tones-based monitoring techniques are data rate and modulation format dependent whereas pilot tones-based schemes are data rate and modulation format independent but inserted pilot tones may interfere with the data signal resulting in BER deterioration.

In digital coherent systems, CD and PMD monitoring can simply be realized by reading off the coefficients of the digital filter in the receiver [25]. Assuming the optical channel is linear with the transfer matrix H(f), the equalization filter W(f) obtained through the zero-forcing (ZF) solution or minimum mean square estimation (MMSE) solution is the inverse impulse response of the channel, expressed as [16]

$$\mathrm{W}(f)=\mathrm{H}^{-1}(f)=D^{-1}(f)\prod_{i=N,-1}^{1}\mathrm{U}_i^{-1}(f)\mathrm{E}_i^{-1} \tag{1.24}$$

where H(f) is composed of the transfer function $D(f)$ and concatenated elements E_i and $\mathrm{U}_i(f)$ accounting for PDL and higher-order PMD. After some algebraic manipulations, the following equations can be obtained

$$\arg(\hat{H}_{\mathrm{CD}}^{-1})=\arg(\sqrt{\det(\mathrm{W}(f))})=-f^2\varphi \tag{1.25}$$

$$\hat{H}_{\mathrm{PDL}}(f)=\left|\sqrt{\det(\mathrm{W}(f))}\right|=\left|H_{\mathrm{AF}}(f)\right|^{-1}\prod_{i=1}^{N}(k_i)^{-1/2} \tag{1.26}$$

$$\mathrm{W}_{UE}(f)=\frac{\mathrm{W}(f)}{\sqrt{\det(\mathrm{W}(f))}}=\prod_i\begin{pmatrix}u_i^* & -v_i\\ v_i^* & u_i\end{pmatrix}\begin{pmatrix}k_i^{1/2} & 0\\ 0 & k_i^{-1/2}\end{pmatrix} \tag{1.27}$$

which are responsible for residual CD, PDL and PMD. $W_{UE}(f)$ is the normalized $W(f)$ by the square root of its determinant. u_i and v_i form the PMD matrices and k_i is the attenuation factor accounting for PDL.

1.3.2. OSNR monitoring

For IMDD systems, several techniques have been proposed for OSNR monitoring such as out-band interpolation [12], polarization nulling [13] and pilot tones inserting [24]. Also, OSNR monitoring can be realized using a delay-line interferometer (DLI) [26] (as shown in Fig. 1.8). Since the signal is coherent and experiences constructive and destructive interference in the DLI whereas in-band noise is non-coherent and insensitive to constructive and destructive interference, the power splitting ratio of signal and noise between the constructive and the destructive ports of the DLI are different. Therefore,

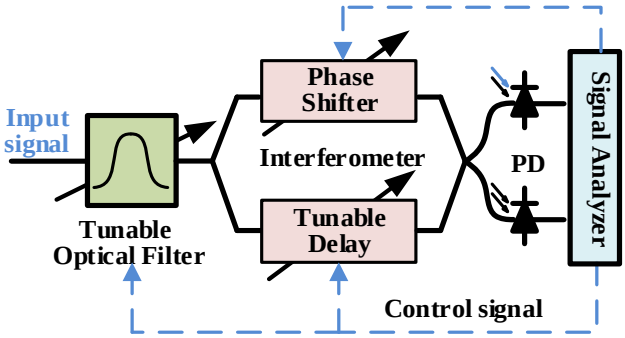

Fig. 1.8 Block diagram of delay-line interferometer (DLI) based OSNR monitor for WDM channels

by measuring the optical power of the constructive and destructive output ports using simple, low-speed photodiodes, the power associated with the signal and the noise can be determined and thus the OSNR can be obtained as,

$$OSNR(dB) = 10\log_{10}\left(\frac{(\alpha+1)\times(\delta-\beta)}{(\beta+1)\times(\alpha-\beta)}\times\frac{\mathrm{NEB}}{0.1\mathrm{nm}}\right), \tag{1.28}$$

where $\alpha=P_{\mathrm{Const,\ Signal}}/\ P_{\mathrm{Dest,\ Signal}}$, $\beta=P_{\mathrm{Const,\ Noise}}/\ P_{\mathrm{Dest,\ Noise}}$, $\delta=P_{\mathrm{Const,\ Channel}}/\ P_{\mathrm{Dest,\ Channel}}$. In the above equation, α, β, and δ are the signal, noise, and channel under test distribution factors, respectively. The NEB is defined as the noise equivalent bandwidth for the filter.

In digital coherent systems, although OSNR monitoring is not as easy as reading off filter taps in the receiver, ASE-noise-induced distortions can be separated from all the other linear transmission impairments by the DSP and reliable OSNR can still be monitored with further processing of the received signals. One simple approach is to utilize the statistical moments of the equalized signal [26]-[30]. The signal used to estimate the OSNR is taken from just after the adaptive equalization, before the carrier phase recovery stage (as shown in Fig. 1.5(b)). The adaptive equalization can either utilize "blind" non-data-aided channel acquisition by gradient algorithms like CMA or data-aided channel acquisition based on a periodically transmitted training sequence. Data-aided channel acquisition gives high estimation accuracy and instantaneous filter acquisition that enables faster OPM with the trade-off of reduced bandwidth efficiency compared to non-data-aided acquisition [31][32].

After adaptive equalization, the linear distortions such as CD and PMD ideally can be fully compensated, and thus the variations of the equalized signal envelope are mainly caused by the ASE noise. We use z_k to represent the envelope of the k^{th} received signal in one particular polarization from the adaptive filter (as shown in Fig. 1.5 (b)). In a practical system, the second- and fourth-order moments from a received data block of L symbols can be calculated as

$$\mu_2 \approx \mathbf{E}(|z_k|^2), \tag{1.29}$$

$$\mu_4 \approx \mathbf{E}(|z_k|^4), \tag{1.30}$$

respectively. $\mathbf{E}(\cdot)$ denotes expectation and the carrier-to-noise ratio (CNR) for QPSK and 16-QAM are expressed as

$$CNR_{QPSK} = \sqrt{2\mu_2^2 - \mu_4} \Big/ \left(\mu_2 - \sqrt{2\mu_2^2 - \mu_4}\right) \tag{1.31}$$

and

$$CNR_{16-QAM} = \sqrt{2\mu_2^2 - \mu_4} \Big/ (\mu_2\sqrt{0.68} - \sqrt{2\mu_2^2 - \mu_4}) \tag{1.32}$$

respectively. When the launched power is so low that fiber nonlinear effects can be neglected, the OSNR value in dB can be estimated from the CNR value as

$$OSNR_{dB} = 10\log_{10}(CNR) + 10\log_{10}(\frac{R_s}{B_{ref}}), \tag{1.33}$$

where R_s is the symbol rate and R_s/B_{ref} is a scaling factor adjusting the measured noise bandwidth to the reference bandwidth B_{ref}. The bandwidth B_{ref} is usually set to 12.5 GHz, which is equivalent to the 0.1-nm OSA resolution bandwidth. As shown in (1.29) and (1.30), measuring second- and fourth-order moments does not include any effect of the phase noise and thus the proposed scheme operates phase insensitively.

All the OSNR monitoring algorithms discussed above for coherent receivers are under the assumption that the optical transmission channel is linear. However, in order to attain the best performance, most of the currently deployed long-haul optical communication systems are operating in the weakly nonlinear regime which is a tradeoff between mitigating the effect of ASE noise and fiber nonlinearities. Nonlinear distortions are typically treated as noise and are indistinguishable from amplifier noise by the standard DSP platform since fiber nonlinearity compensation algorithms such as digital back-propagation [33] is too complex to be realized at present. Therefore, those abovementioned OSNR estimation techniques based on the SNR of equalized signal will considerably under-estimate the OSNR for long-haul transmission systems and nonlinearity-insensitive OSNR monitoring techniques are still highly desirable.

1.4. Transmission Strategies for Long-haul Digital Coherent Systems in Presence of Fiber Nonlinearity

Fiber-optic communication capacities have be significantly improved by the advances made over the past decade in digital coherent systems with advanced modulation formats, error-control coding and powerful DSP capable to fully mitigate linear channel response. However, fiber-optic communication infrastructure continues to be under extreme pressure because of exponentially growing bandwidth demands driven by the increasing traffic volumes of cloud services, online gaming, internet of things, etc. Since the Kerr effect in optical fibers induces nonlinear waveform distortion and strictly limits the maximum launched optical power and thus the OSNR, current fiber-optic systems comes to a point where nonlinearity becomes the limiting factor [34].

Fiber nonlinearity compensation (NLC) based on DSP is a potential technique that allows further transmission capacity improvement. Several NLC techniques have been proposed over last several years, including electronic pre-distortion [35], optical phase conjugation (OPC) [36], digital back propagation (DBP) [33][37] etc, among which DBP is the most representative and widely investigated NLC technique.

1.4.1. Nonlinearity Compensation using Digital Back Propagation

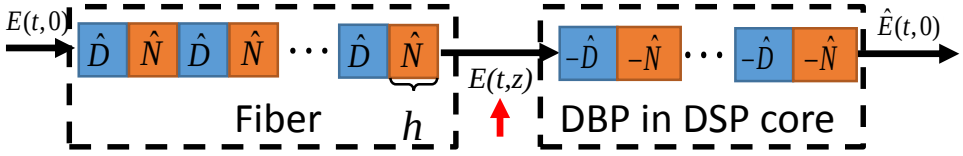

Fig. 1.9 Concept of digital back propagation

Digital back propagation is a digital NLC technique that iteratively solves the nonlinear Schrödinger equation using split-step Fourier method and can be deployed either at the transmitter or receiver, or both. Basically, the DSP can undo the Kerr-induced distortion by conducting virtual back-propagation in the digital domain, as shown in Fig. 1.9. First, the forward signal propagation process in fiber is divided into short segment of length h and each segment is considered as the concatenation of (separable) nonlinear and linear step (split-step Fourier method). After coherent detection, the received

signal is processed by the DSP that emulates the signal transmission through virtual fibers having the inverse characteristics (opposite signs) of the actual transmission link as,

$$E(t, z_0 + h) = F^{-1}\underbrace{\left\{ \underbrace{F\left\{E(t, z_0)\exp(j\gamma |E(t, z_0)|^2 h)\right\}}_{\text{nonlinear step } \hat{N}} \exp\left(j\frac{\beta_2}{2}\omega^2 h \right)\right\}}_{\text{linear step } \hat{D}}, \quad (1.34)$$

where $F\{\cdot\}$ is the Fourier transform operator. Equation (1.34) literally represents the back propagation of the signal, as opposed to forward fiber propagation. With this approach, deterministic transmission impairments such as CD and the Kerr effects can be undone simultaneously and thus the input signal can be restored in the DSP core.

Theoretically, in the absence of noise, DBP can full compensate all the deterministic channel impairments including inter-channel nonlinearities such as XPM and FWM when the joint transmission and detection are assumed [38][39] which might be possible in case of a point to point link. However, in a meshed network, it is not generally possible to perform joint transmission and detection since many signals join and leave the optical link in intermediate nodes without even being noticed by other users and thus the information from neighboring traffic channels is practically unavailable. As a result, the interference introducing from these signals is unavoidably treated as noise and limits the gain of such NLC technique. Additionally, inter-channel nonlinear interactions strongly depend on the polarization state of each channels and for typical values of the PMD parameter, multichannel DBP becomes ineffective as the back-propagation bandwidth increases [40]. Furthermore, the computational complexity of DBP is extremely high even considering signal channel compensation [41]. Therefore, it is not considered practical from implementation view point unless there is an improved algorithm that provides efficient compensation at a relatively low computational cost.

1.4.2. Nonlinear Frequency Division Multiplexed Transmission Based on Nonlinear Fourier Transform

Most current NLC approaches such as DBP and electronic pre- and post-compensation assume a linearly dominated regime of operation, or consider the nonlinearity as a small perturbation, and

towards to manage and suppress the (detrimental) effects of the nonlinear and dispersive terms [33][35]. However, their performance gain is severely limited by noise-nonlinearity interactions and inter-channel nonlinearities as the lack of information from other channels. It is generally acknowledged that current fiber-optic transmission technologies borrowed from wireless communication, where the channel transfer function is linear, will not be capable of meeting the customer bandwidth demand within the next decade.

Yousefi and Kschischang [42]-[44] recently revived the theoretical framework of nonlinear Fourier transform (NFT) and adopted nonlinear frequency division multiplexing (NFDM) as a new signaling scheme, a totally different philosophy that is fundamentally compatible with fiber nonlinearity and dispersion, rather than treating them as nuisances.

Let's take a second look at the Eq (1.1). In the NLSE, the signal degrees-of-freedom couples together via the nonlinearity and dispersion in a complicated manner among propagation in optical fibers, making it difficult to establish the channel input-output map, even deterministically. However, by changing the variables through

$$q = \frac{E}{\sqrt{2/\gamma}}, \qquad z = Z/L, \qquad t = T/\sqrt{|\beta_2| L/2}, \tag{1.35}$$

and omit the loss term if ideal distributed Raman amplification is assumed, the NLSE is normalized to,

$$jq_z(t,z) = q_{tt}(t,z) + 2|q(t,z)|^2 q(t,z), \tag{1.36}$$

and becomes integrable that can be "diagonalized" with the help of the NFT, a powerful tool that can solve integrable nonlinear dispersive partial differential equations effectively [42].

With the help of the NFT, a signal can be represented by its nonlinear spectra, a function of distance z and the complex-valued frequencies λ, which can be divided into discrete part $\tilde{q}(z,\lambda_j)$ and continuous part $\hat{q}(z,\lambda)$:

$$\begin{cases} \hat{q}(z,\lambda) = \dfrac{b(z,\lambda)}{a(z,\lambda)}, & \lambda \in \mathbb{R}, \\ \tilde{q}(z,\lambda_j) = \dfrac{b(z,\lambda_j)}{a'(z,\lambda_j)}, & \lambda_j \in S \subset \mathbb{C}^+, \end{cases} \tag{1.37}$$

where the prime denotes differentiation and S is the set of the (isolated) zeros of the analytic function

a(λ) in the upper half complex plane $\mathbb{C}^+$, called eigenvalues. In this thesis, we limit our study of NFDM systems with discrete eigenvalues only.

While the optical signal propagates along the fiber based on the complicated NLSE, the action of the channel on its spectral components will actually translate to the nonlinear Fourier coefficients as [42]

$$\hat{q}(z,\lambda) = \hat{q}(0,\lambda) \cdot e^{-j4\lambda^2 z}, \qquad \tilde{q}(z,\lambda_j) = \tilde{q}(0,\lambda_j) \cdot e^{-j4\lambda^2 z}. \tag{1.38}$$

Since the nonlinear Fourier coefficients after propagation simply undergo a multiplicative factor $e^{-j4\lambda^2 z}$ and they do not mutually interfere, the mathematical structure is identical to how one encode information in the frequency spectrum, or multiple sub-carriers, of OFDM signaling. Therefore, one can think of encoding information in the NFT coefficients and they will not interfere with each other upon propagation along the fiber. Under this framework, like the (ordinary) Fourier transform converting a linear convolutional channel $y(t) = x(t) * h(t)$ into a number of parallel scalar channels, the NFT converts a nonlinear dispersive channel described by NLSE into a number of parallel scalar channels having the "nonlinear transfer function",

$$H(\lambda) = e^{-j4\lambda^2 z}. \tag{1.39}$$

This new transmission strategy is called nonlinear frequency division multiplexing and its concept is shown in Fig. 1.10.

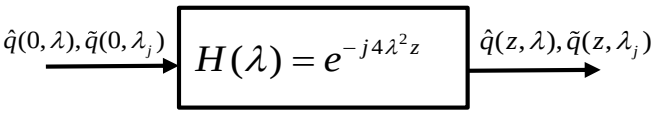

Fig. 1.10. The concept of NFDM transmission based on the NFT.

As a fundamentally new signaling scheme, NFDM is intrinsically compatible with fiber nonlinearity and thus potentially may be a fundamental paradigm shift in long-haul WDM optical communications and may show a way to operate beyond fiber's nonlinear capacity limit. The theory of NFT and NFDM will be discussed in more details in Chapter 4.

1.5. Research Objective and Organization of the Thesis

The fundamental technology shift brought about by digital coherent systems determines the roles, functionalities and research objectives of optical performance monitoring (OPM) and long-haul transmission strategies: 1) Since all the linear impairments such as chromatic dispersion (CD) and polarization-mode dispersion (PMD) can be estimated and fully compensated by numerous DSP algorithms in the digital coherent receiver, OSNR becomes the performance-limiting factor of coherent systems and hence OSNR monitoring is most vital for coherent links. 2) Because of Kerr nonlinearities, current fiber-optic transmission technologies designed for linear channels will not be capable of meeting the customer bandwidth demand even equipped with nonlinear compensation techniques. Therefore, to develop OSNR monitoring techniques and nonlinearity-compatible transmission strategies for long-haul digital coherent systems will be the research objectives of this thesis.

Chapter 1 presents the background, motivation and organization of the dissertation. The channel impairments in fiber links including both linear and nonlinear ones are introduced. The advances of coherent systems comparing to non-coherent systems are discussed. The objectives and challenges of OPM techniques for coherent systems are discussed. At last nonlinear compensation techniques and newly developed nonlinearity-compatible NFDM systems are introduced.

In chapter 2, a fiber nonlinearity-insensitive OSNR monitoring based on the received signal distributions after CPE is proposed. The nonlinearity-induced amplitude noise correlation across neighboring symbols are characterized and incorporated into error vector magnitude (EVM) calculation to realize calibration. Accurate and nonlinearity-insensitive OSNR monitoring is experimentally demonstrated for 112 Gb/s PM-QPSK systems and simulatively demonstrated for 224 Gb/s PM-16-QAM systems. Tolerance of the proposed OSNR monitoring technique to different pulse shapes, timing phase offsets, PMD, PDL and WDM effects are also investigated through simulations.

In chapter 3, a low-cost OSNR monitoring scheme utilizing reduced-complexity coherent receptions, electrical filtering and RF power measurements is proposed and experimentally demonstrated. By measuring the RF power of the coherently received baseband signals at three different frequency components, the proposed OSNR monitor is also insensitive to spectral narrowing induced by cascaded WSSs. Accurate data-format-transparent and filtering-effect-insensitive OSNR monitoring

for 25-Gbaud polarization multiplexing transmissions with QPSK, 16-QAM and 64-QAM signals over various distances with different amount of filtering effects by cascaded WSSs. The influence of different system parameters, such as the bandwidth of the electrical low-pass filter, the laser frequency offset and laser linewidth on the accuracy of the proposed OSNR monitor are characterized. The robustness of the proposed OSNR monitoring scheme to fiber nonlinearities, calibration parameter mismatches and variations of WSS parameters are also investigated.

In chapter 4, we experimentally demonstrate for the first time the successful simultaneous and independent modulation of 3- and 4-eigenvalue multi-soliton NFDM signals. Error-free 3-eigenvalue transmission over 1800 km and 4-eigenvalue transmission over 200km of standard single-mode fiber with Raman amplification and coherent detection are demonstrated. The impact of frequency offset and laser phase noise on the multi-eigenvalue OOK NFDM systems are also investigated. Simulation results show that OOK modulated NFDM systems are robust to the frequency offset and laser phase noise in a certain range.

Chapter 5 summarizes the work performed and identifies some possible research directions for future works.

Chapter 2

OSNR Monitoring for QPSK and 16-QAM Systems in presence of Fiber Nonlinearity for Digital Coherent Receivers

2.1. Introduction

OPM is especially critical to assess the quality of transmission link and system performance that facilitate link fault localization with fast protection path switching. Since linear impairments such as CD and PMD can be fully compensated in coherent systems by numerous DSP algorithms [2], system performance is largely determined by the OSNR and hence OSNR monitoring is especially vital for such systems. Techniques based on optical spectral analysis [45], polarization nulling [12], asynchronous histograms [46] and neural networks [47] among others have been proposed for OSNR monitoring. However, some of these methods are only applicable to certain modulation format/pulse shapes and are not applicable to polarization-multiplexing systems. In addition, they may not work in realistic communication systems where other deterministic and statistical channel impairments are present.

Advanced coherent modulation formats such as PM-QPSK and PM-16-QAM with digital coherent receivers and appropriate transmission impairment compensation algorithms have emerged as the most promising solution for the next generation high capacity optical transmission networks operating at 100-Gbps and beyond [2][25]. It also enables a promising and comprehensive built-in optical performance monitor at the receiver for free. CD, PMD and PDL can be estimated through analyzing the filter impulse response which is an indicator of the inverse impulse response of the channel [14][16]. Meanwhile, although OSNR monitoring is not as easy as reading off filter taps, ASE-noise-induced distortions can be separated from all the other linear transmission impairments in a digital coherent receiver and reliable OSNR can still be estimated with further processing of the received signals. Pittal à proposed an OSNR monitoring technique [32] through data-aided FD channel estimation employing very short training sequences. Other methods are derived from wireless communications including the

estimation of OSNR through the moments of the radial distribution of equalized PM-QPSK signals in digital coherent receivers [26] or using EVM for non-data-aided receivers [48]. However, most of the currently deployed long-haul optical communication systems operate in the weakly nonlinear regime which is a tradeoff between mitigating the effect of ASE noise and fiber nonlinearities. The OSNR increases with the signal launched power but so does the impact of fiber nonlinearities. Nonlinear distortions are typically treated as noise and are indistinguishable from amplifier noise by the standard DSP platform [49] since fiber nonlinearity compensation algorithms such as digital back-propagation [33][37] is too complex to be realized at present. Therefore, current OSNR estimation techniques using digital coherent receivers will considerably under-estimate the OSNR for long-haul transmission systems and a fiber-nonlinearity-insensitive OSNR monitoring technique is yet to be developed to realize accurate OSNR monitoring in long-haul optical communication systems.

In this chapter, we propose to use the received signals after CPE in a standard digital coherent receiver and characterize the fiber nonlinearity induced amplitude noise correlation among neighboring symbols as a quantitative measure of nonlinear distortions to the signal. This nonlinear measure is shown to only depend on signal launched power but not OSNR and hence fiber nonlinear distortions can be isolated from ASE noise. In this case, nonlinearity-insensitive OSNR monitoring can be achieved by incorporating/calibrating such amplitude noise correlations into an EVM-based OSNR estimator. Experimental as well as simulation results demonstrate an OSNR monitoring range of 10-24 dB with a maximum estimation error of 1.0 dB for 112 Gb/s PM-QPSK systems and 18-28 dB with a maximum estimation error of 1.0 dB for 224 Gb/s PM-16-QAM systems. The maximum signal launched power is 4 dBm for transmission distance up to 800 km and 2 dBm for longer distance up to 1600 km. It should be noted that signal launched power above 2 dBm at such transmission distances are already considerably higher than the optimal signal power level for realistic 28G baud PM-QPSK and PM-16-QAM systems [50][51] and hence the proposed technique is applicable to systems with strong fiber nonlinearity. In addition, the proposed OSNR monitoring technique is shown to be tolerant towards the effects of timing phase offsets, different signal pulse shapes, PDL and first-order PMD. Furthermore, simulations for WDM systems show that while inter-channel nonlinearities such as cross-

phase modulation (XPM) can introduce further distortions to the signal, appropriate calibrations to the proposed OSNR estimator can be performed to maintain the OSNR monitoring accuracy.

2.2. Theoretical Foundations

2.2.1. OSNR Estimation based on Received Signal Distributions and EVM

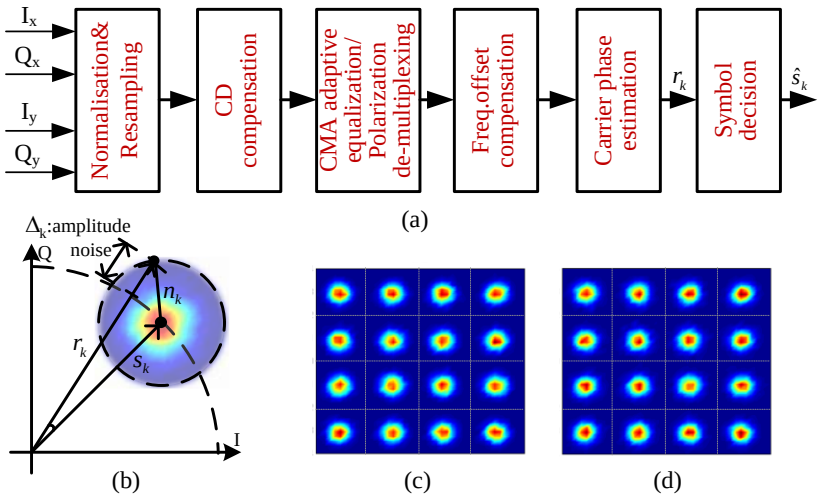

Fig. 2.1. (a) Standard signal processing blocks in a digital coherent receiver; (b) Graphical illustration of received signal and amplitude noise Δ_k ; Received 16-QAM distributions with (c) -4 dBm signal launched power and 18 dB OSNR (d) 4 dBm signal launched power and 26 dB OSNR over a 800-km link. As evident from the figures, amplifier noise and fiber nonlinearity effects will induce similar distortions to the received signal distribution and therefore it is not easy to distinguish between them for accurate OSNR monitoring.

Consider a coherent optical transmission system with a polarization-multiplexed *M*-QAM signal transmitted over a multi-span link with inline optical amplifiers to compensate for signal loss incurred throughout the span. Transmission impairments such as CD, PMD, fiber nonlinearity and ASE noise generated from inline amplifiers will distort the received signal and possibly limit system performance. Neglecting electrical noise generated from receiver circuitries, fiber nonlinearity and multi-channel effects, the received signal in a digital coherent receiver is sampled and processed in a DSP unit with standard signal processing algorithms such as normalization, re-sampling, CD/PMD compensation, laser frequency offset and carrier phase estimation as shown in Fig. 2.1(a). In this case, the k^{th} received symbol of the CPE output in one particular polarization can be represented as

$$r_k = s_k + n_k \tag{2.1}$$

where s_k is the transmitted *M*-QAM symbol and n_k models the collective ASE noise generated by inline optical amplifiers which is a band-limited complex circularly symmetric zero-mean Gaussian random process with covariance matrix $\sigma^2 I$. Many techniques exist to estimate OSNR from r_k. In particular, we use the principle of EVM in [48] and propose an OSNR estimate through

$$OSNR_{Estimated} = \frac{P_{in}}{P_{ASE}} = \frac{\mathbf{E}(|\hat{s}_k|^2)}{\mathbf{E}(|n_k|^2)} \tag{2.2}$$

where P_{in} is the signal power, P_{ASE} accounts for the ASE noise power and $\hat{s}_k$ is the symbol after decision as shown in Fig. 2.1(a) and $\mathbf{E}(\cdot)$ denotes expectation.

However, in realistic long-haul transmission systems where fiber nonlinearity impairs system performance, the interaction of nonlinearity, CD and ASE noise results in additional distortions that cannot be easily mitigated by standard DSP techniques. Recently, a zero-mean complex circularly symmetric additive Gaussian model for such nonlinear distortions has been analytically proposed and experimentally validated [52][53] for long-haul coherent transmission links without in-line dispersion compensation. At a high baud rate, i.e. 28G baud/s, optical pulses are largely overlapped due to CD and it can be shown that intra-channel nonlinearities such as intra-channel four-wave mixing (IFWM) dominate over inter-channel nonlinearities such as XPM [54][55]. Considering the effect of intra-channel nonlinearity only, (2.1) can be re-written as

$$r_k = s_k + n_k' = s_k + n_k + v_k \tag{2.3}$$

where $n_k' = n_k + v_k$ consists of ASE noise n_k and nonlinearity-induced distortions v_k. With the EVM methodology, v_k become addition distortions that can significantly affect the OSNR estimate from the received signal distributions. Fig. 2.1(c) and (d) shows the received signal distributions obtained from simulations for a 224 Gb/s PM-16-QAM signal transmitted over 800 km of SSMF where the signal launched power (OSNR) are -4 dBm (18 dB) and 4 dBm (26 dB) respectively. It is clear from the figures that despite the difference in OSNR, fiber nonlinearity effects result in additional distortions and can become indistinguishable from ASE noise. Thus if we naively use the EVM method by simply

measuring the 'size' of the 'clouds' in the received signal distributions, the OSNR estimates are given by

$$OSNR_{Estimated} = \frac{\mathbf{E}(|\hat{s}_k|^2)}{\mathbf{E}(|n'_k|^2)} = \frac{\mathbf{E}(|\hat{s}_k|^2)}{\mathbf{E}(|n_k|^2) + \underbrace{\mathbf{E}(|v_k|^2) + \mathbf{E}(n_k v_k^*) + \mathbf{E}(n_k^* v_k)}_{P_{NL}}} = \frac{P_{in}}{P_{ASE} + P_{NL}} \quad (2.4)$$

which can significantly under-estimate the true OSNR. Consequently, techniques to isolate fiber nonlinearity effects from ASE noise are to be developed in order to realize accurate OSNR monitoring in coherent links in presence of fiber nonlinearity.

2.2.2. Calibrating Nonlinearity Induced-amplitude Noise Correlations across Received Symbols into EVM-based OSNR Estimates

The interaction of fiber nonlinearity, CD and ASE noise will produce distortions such as IFWM that are shown to be correlated across neighboring symbols even after appropriate linear impairment compensation [56]. In particular, the phase as well as amplitude noise across neighboring symbols are shown to be correlated. Denoting Δ_k as the amplitude noise of the k^{th} received symbol, let the autocorrelation function (ACF) of amplitude noise across neighboring symbols be

$$R_\Delta(m) = \mathbf{E}[\Delta_k \Delta_{k+m}] \quad (2.5)$$

Fig. 2.2 compares $|R_\Delta(m)|$ of a 112 Gb/s PM-QPSK system and a 224 Gb/s PM-16-QAM system obtained from simulations for various signal launched powers and OSNR values. The transmission distance is 800 km without inline optical CD compensation and the received signals are sampled and processed by standard signal processing blocks depicted in Fig. 2.1(a) and the amplitude noise autocorrelation are calculated accordingly from the received signal distribution after carrier phase estimation. From the figure, it is clear from $|R_\Delta(m)|$ that the amplitude noise is correlated across neighboring symbols. Also, as $|R_\Delta(0)|$ is basically the amplitude noise variance in each received symbol, it would vary with both signal launched power and OSNR as reflected in the figure. However, $|R_\Delta(1)|, |R_\Delta(2)|, |R_\Delta(3)| \cdots$ seem to only depend on signal launched power and is quite insensitive to

OSNR. This can be explained as follows: with appropriate optical and electrical filtering in a transmission link, ASE noise n_k of the received symbols r_k should be uncorrelated across neighboring symbols. However, CD induces pulse overlapping during transmission and the pulses interact with each other through fiber nonlinearity and consequently result in additional nonlinear distortions v_k in r_k. As v_k originates from neighboring symbols, it is intuitive to expect that v_k is correlated across neighboring symbols and such correlations are largely attributed to nonlinear interactions between signal pulses rather than signal-ASE noise or ASE noise-ASE noise interactions.

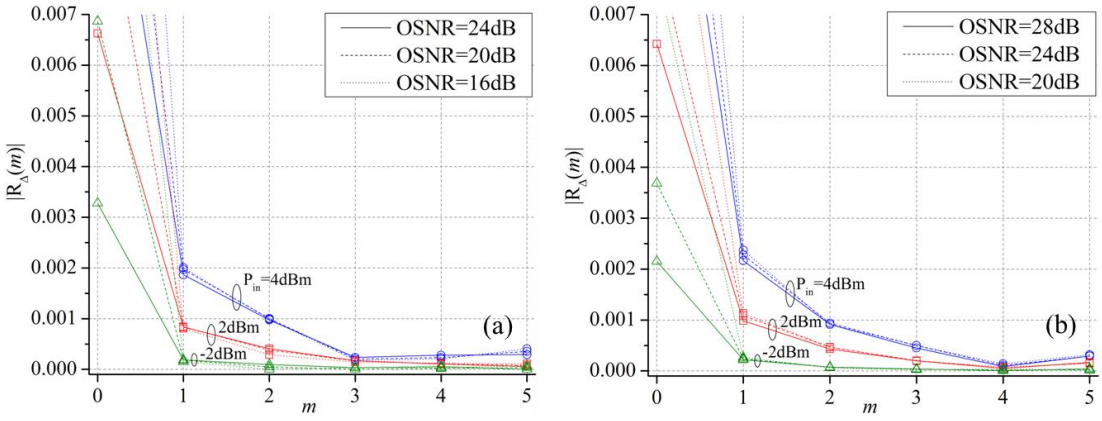

Fig. 2.2. Autocorrelation of fiber-nonlinearity induced amplitude noise $|R_\Delta(m)|$ for a (a) 112 Gb/s PM-QPSK system and (b) 224 Gb/s PM-16-QAM system with various signal launched powers and OSNR values. The transmission distance is 800 km without inline optical CD compensation and the received signals are sampled and processed by standard DSP blocks depicted in Fig. 2.1 (a) and the amplitude noise autocorrelation are calculated accordingly from the received signal distribution after carrier phase estimation. From the figure, $R_\Delta(1)$ only depends on signal launched power and is insensitive to ASE noise and hence can be used to isolate fiber nonlinearity effects from ASE noise.

With such observation and insight, one can leverage the unique properties of $|R_\Delta(m)|$ to isolate nonlinear distortions from ASE noise and realize fiber-nonlinearity-insensitive OSNR monitoring. In particular, one can use $|R_\Delta(1)|$ multiplied by a calibration factor ξ as a measure/estimate of the amount of nonlinear distortions P_{NL} in the received signal r_k. The calibration factor ξ only depends on the transmission distance L and is optimized over different signal launched powers and OSNR values by the following calibration process: 1) Obtain received signal data set (through simulations or

experiments) for various launched powers and OSNR values; 2) Calculate OSNR through Eq. (6) as a function of ξ for each launched power and OSNR value; 3) Optimize ξ so that the maximum monitoring error for the whole data set is minimized. 4) Store the optimized ξ (as a function of distance) in a look-up table which will be used in the actual monitoring process. We simulated an 800-km CD-uncompensated link with standard receiver DSP blocks shown in Fig. 2.1(a). The ACF $|R_{\Delta}(m)|$ is calculated from r_k and $\hat{s}_k$ accordingly and Fig. 2.3 compares $|R_{\Delta}(1)|\times\xi$ with P_{NL} for various signal launched powers and OSNR values. With an optimally chosen ξ, we can see that the $|R_{\Delta}(1)|\times\xi$ closely estimate P_{NL} and are quite insensitive to different OSNR values. Similar results are obtained for PM-16-QAM systems but will be omitted here.

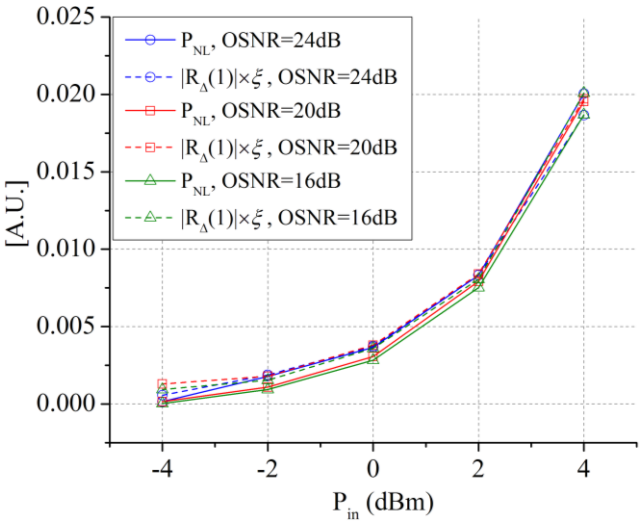

Fig. 2.3. $|R_{\Delta}(1)|\times\xi$ and nonlinear noise power P_{NL} as a function of signal launched power in a 800-km CD uncompensated link. The optimal ξ is calibrated to be 10.2.

The term $|R_{\Delta}(1)|\times\xi$ is incorporated in the OSNR estimator in (2.2) and thus a nonlinearity-insensitive OSNR estimation can be obtained by

$$OSNR_{Estimated} = \frac{\mathbf{E}(|\hat{s}_k|^2)}{\mathbf{E}(|n'_k|^2) - |R_{\Delta}(1)|\times\xi} \quad . \tag{2.6}$$

It should be noted that the received signals in both polarization multiplexed tributaries are used for the OSNR estimation in (2.6). Moreover, phase noise correlation can also be used to calibrate and

estimate P_{NL} and serve the same purpose of realizing accurate OSNR monitoring in presence of fiber nonlinearity. We choose to use amplitude noise correlation instead because of its robustness against additional phase noise effects such as laser frequency offsets and laser phase noise and corresponding DSP techniques to mitigate them might not be perfect in practice.

2.3. Experimental and Simulation Results for 112 Gb/s PM-QPSK and 224 Gb/s PM-16-QAM Systems

2.3.1. Experimental Results for 112 Gb/s PM-QPSK Systems

Experiments have been performed to demonstrate the validity of the proposed OSNR monitoring technique for 112 Gb/s PM-QPSK systems. The experimental configuration is shown in Fig. 2.4. At the transmitter side, an ECL laser at 1550.12nm is modulated with an I/Q modulator driven by 28G baud pseudo random bit sequences (PRBS) of length 2^{31}-1 to produce NRZ QPSK signals. Polarization division multiplexing is achieved by splitting the signal through a polarization beam splitter (PBS) into two branches, delaying one branch, and recombining the signal through a polarization beam combiner (PBC). The signal is then amplified and launched into the fiber recirculating loop with a transmitted power ranging from -4 to 4 dBm to realize various levels of fiber nonlinearity. The loop consists of a span of 80 km SSMF, EDFA, an attenuator placed before the EDFA to realize various OSNR values from 10 to 24 dB and also a 5nm optical band- pass filter (BPF) for channel power equalization. At the loop output, ten percent of the light is taped into an optical spectrum analyzer (OSA) to obtain the reference (true) OSNR using out-of-band noise measurement [57]. Here and throughout the chapter, the OSNR will be referred to the 0.4 nm bandwidth which corresponds to the whole signal bandwidth. The rest of the signal is filtered by a 3th order Gaussian optical BPF having 0.4 nm bandwidth and enters an integrated coherent receiver. The linewidth of transmitter and local oscillator (LO) are 150 kHz and 100 kHz respectively and the frequency offset is set to be 1 GHz. The coherently detected signal are sampled by a 50 G samples/s real-time oscilloscope and then processed offline with the following DSP algorithms: 1) Normalization and resampling to 2 samples/symbol; 2) Chromatic dispersion compensation using a finite impulse response filter [2]; 3) Adaptive equalization/PMD

compensation/polarization de-multiplexing with CMA [2]; 4) Frequency offset compensation and carrier phase estimation [2]; 5) Symbol decision, amplitude noise correlation calculation through (2.5) and OSNR estimate through (2.6). In our experiments, 100000 symbols are used for the OSNR estimation which only requires an acquisition time of a few microseconds.

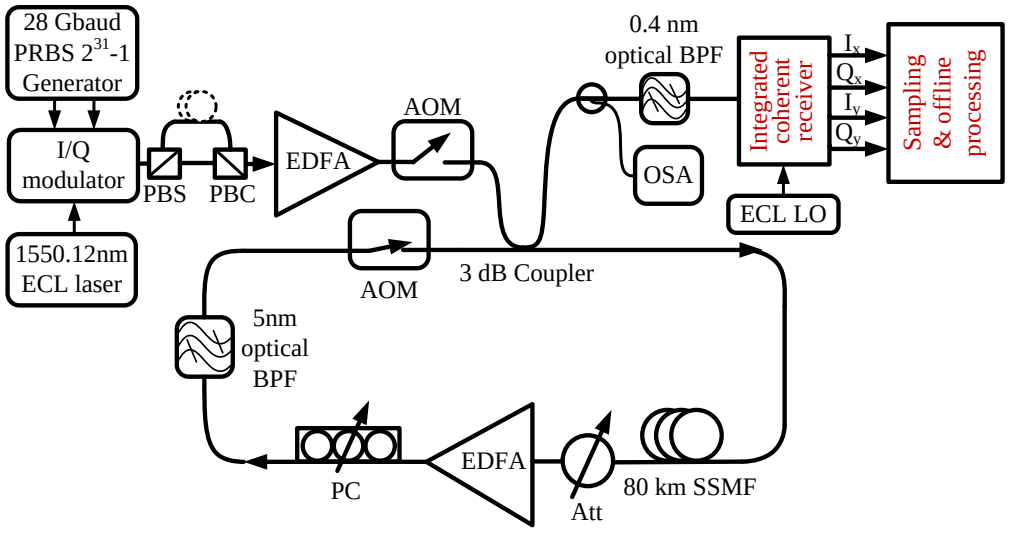

Fig. 2.4. System configuration for a 112Gbit/s PM-QPSK system without inline dispersion compensation. Att: attenuator, AOM: acousto-optic modulator, BPF: band-pass filter, ECL: external cavity laser, EDFA: erbium-doped fiber amplifier, PBS: polarization beam splitter, PBC: polarizing beam combiner, PC: polarization controller, OSA: optical spectrum analyzer, SSMF: standard single-mode fiber.

It is well known that practical systems suffer from impairments such as imperfect matching filters and transceiver imperfections which introduce additional distortions to the received signal. We first conducted a back-to-back experiment to estimate and 'calibrate out' such imperfections [26][53].

With the received symbols obtained from experiments, the autocorrelation of fiber nonlinearity-induced amplitude noise are shown in Fig. 2.5 and the OSNR estimates before and after calibration with $|R_{\Delta}(1)|\times\xi$ are shown for comparisons in Fig. 2.6. For each transmission distance, the same calibration factor ξ obtained as described in the previous section is used for all the measurements and recalibration is not required. When $|R_{\Delta}(1)|\times\xi$ is not incorporated, the OSNR is significantly under-estimated as the nonlinear distortions are treated as ASE noise in the OSNR estimates and the estimation error generally increases with input power due to enhanced nonlinearity effects. With the

calibration based on $|R_{\Delta}(1)|\times\xi$, the OSNR estimation error is largely reduced and the maximum errors are 0.82 dB, 0.93 dB, 0.77 dB and 1.0 dB for 400 km, 800 km, 1200 km and 1600 km transmissions respectively. The dependence of the optimized ξ on transmission distance is shown in Fig. 2.7 where it generally increases with distance. This is to be expected as nonlinear effects are known to build up with transmission distance [53]. It should be noted that signal launched power above 2 dBm are considerably higher than the optimal signal power level for realistic 28G baud PM-QPSK and PM-16-QAM systems [50][51], thus illustrating the proposed technique will still function well in highly nonlinear systems.

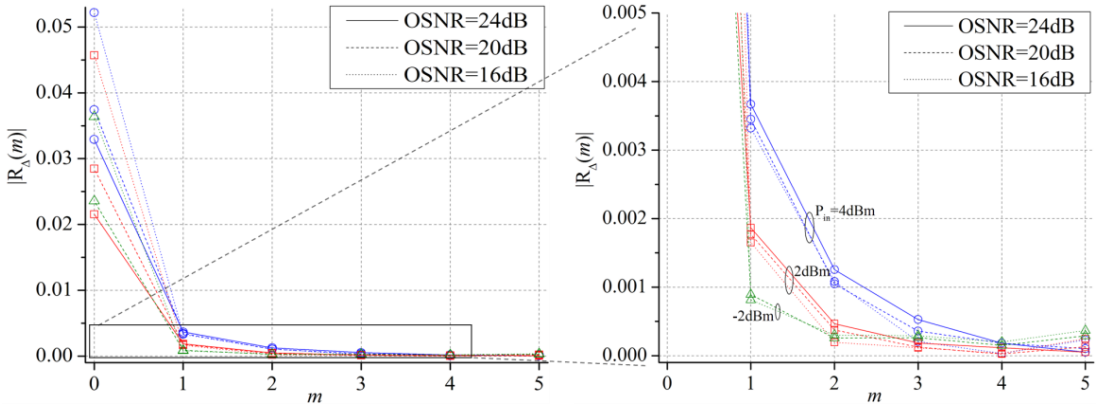

Fig. 2.5. Autocorrelation of fiber nonlinearity-induced amplitude noise experimentally obtained from a 112 Gb/s PM-QPSK system in a 800-km CD uncompensated link with standard DSP algorithms for transmission impairment compensation for various signal launched powers and OSNR values.

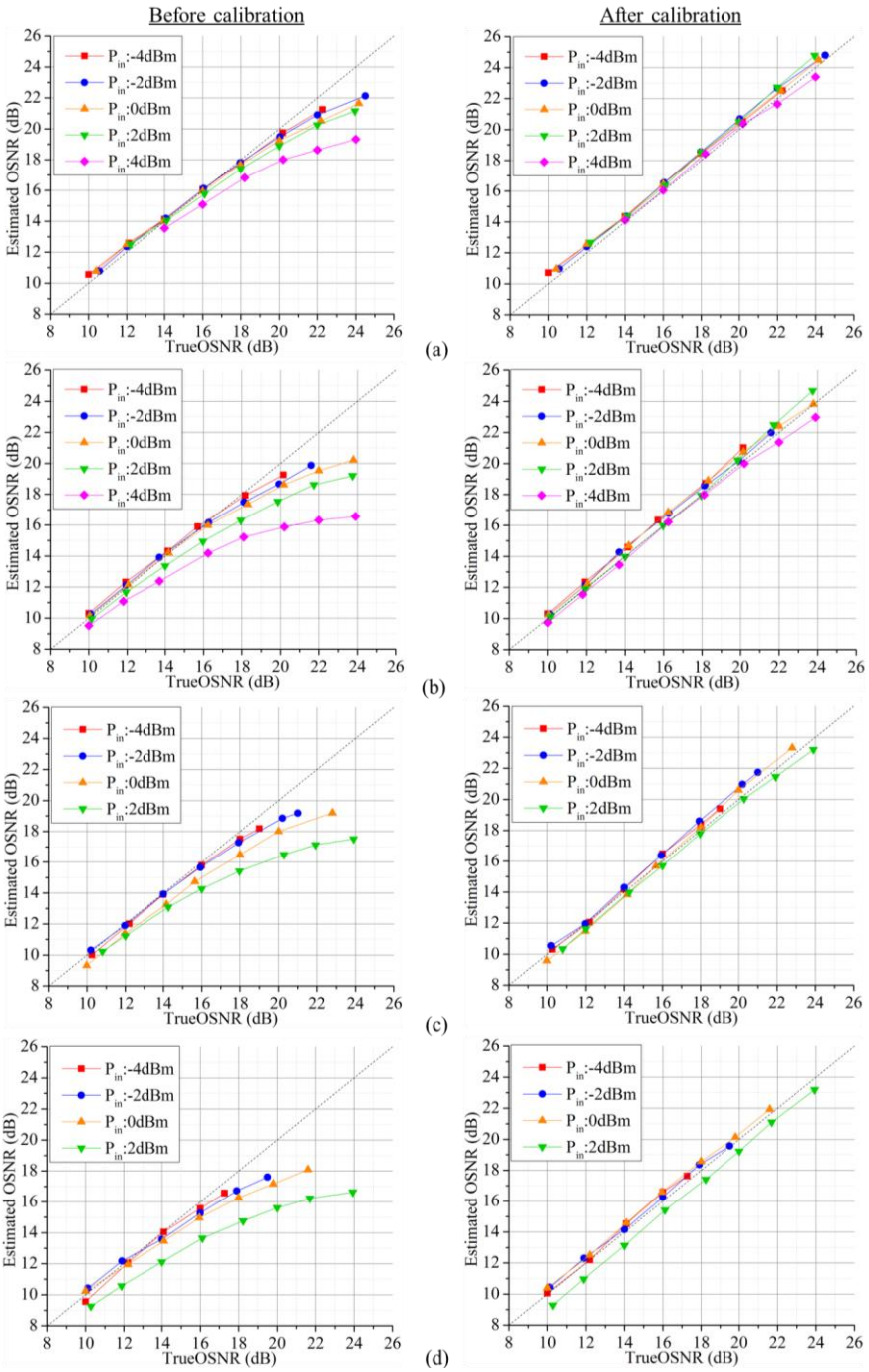

Fig. 2.6. Estimated OSNR vs true OSNR experimentally obtained from a 112 Gb/s PM-QPSK system for various signal launched powers and OSNR values (a) after 400 km transmission and calibrated with ξ=9. The maximum estimation error is 0.82 dB; (b) after 800 km transmission and calibrated with ξ=10.5. The maximum estimation error is 0.93 dB; (c) after 1200 km transmission and calibrated with ξ=11.5. The maximum estimation error is 0.77 dB; (d) after 1600 km transmission and calibrated with ξ=12.5. The maximum estimation error is 1.0 dB.

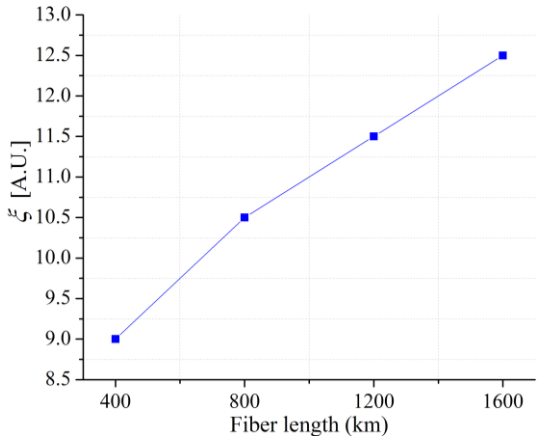

Fig. 2.7. The optimized calibration factor ξ vs. transmission distance for a 112 Gb/s PM-QPSK system for realizing nonlinearity-insensitive OSNR monitoring.

2.3.2. Simulation Results for 224 Gb/s PM-16-QAM Systems

For 224 Gb/s PM-16-QAM systems, simulations using VPI [58] are performed to demonstrate the validity of the proposed OSNR monitoring technique. In the simulation setup, the 16-QAM signals are generated by a four-level-driven I/Q modulator at the transmitter side. In the receiver DSP, the cascaded multi-modulus algorithm (CMMA) [59] is added after the standard CMA to better equalize the 16-QAM signals and the CPE algorithm reported in [60] is used. The rest of system setup is similar to that shown in Fig. 2.4.

In order to investigate the robustness of the proposed OSNR monitoring technique against different signal pulse shapes, timing phase offsets, PDL and first-order PMD effects, we studied the performance of our proposed OSNR monitor in NRZ-PM-16-QAM and 50% Return-to-Zero (RZ)-PM-16-QAM systems and a fiber link with PDL ranging from 0 to 4 dB (with 0° and 45° angles between signal state of polarization (SOP) and PDL axis) using the distributed PDL model described in [61] and DGD values ranging from 0 to 20 ps (with 0°, 22.5° and 45° angles between signal SOP and fiber PSP. The timing phases considered include 0, 1/8, 1/4 and 3/8 symbols away from optimal sampling instants at the pulse peaks.

More than a hundred OSNR monitoring curves corresponding to various pulse shapes, timing phase offsets, PDL and PMD values are generated by simulations. For each transmission distance, the calibration factor ξ has been optimized over different launched powers, OSNRs, pulse shapes, PDL

and PMD effects for optimal OSNR estimation performance. Typical OSNR estimation results before and after calibration are shown in Fig. 2.8. For an OSNR monitoring range from 18 to 28 dB, the maximum monitoring errors are 0.35 dB, 0.94 dB, 0.53 dB and 1.0 dB for 400 km, 800 km, 1200 km and 1600 km transmissions respectively when PDL and PMD effects are absent. The maximum monitoring errors become 0.5 dB, 1.1 dB, 0.82 dB and 1.18 dB respectively when PDL is present. PMD further increases the maximum monitoring errors to 0.9 dB, 1.73 dB, 1.81 dB and 1.98 dB for 400 km, 800 km, 1200 km and 1600 km transmissions respectively. The increased estimation errors are partly due to the OSNR monitoring range shifting to higher values where the ASE noise is relatively small and thus the monitoring performance is more vulnerable to the other distortions such as PMD. However, the estimation errors still remain on a reasonably low level and illustrates that our technique is applicable to different pulse shapes and rather insensitive to PDL and PMD effects. We would like to note that the effect of PMD on our proposed OSNR monitoring technique can potentially be further reduced by first determining the angle between SOP and PSP and the DGD value from the CMA/CMMA taps and calibrate a factor ξ specific to different angles and DGD values. All in all, the proposed technique is robust against typical PMD and PDL effects.

The optimized calibration factor ξ versus transmission distance is shown in Fig. 2.9. It should be noted that ξ is not transmission distance independent as shown in Fig. 2.7 and Fig. 2.9 and thus in some cases, i.e. in reconfigurable optical systems where the transmission distance varies, inaccurate estimation of transmission distance may affect the OSNR measurement accuracy. For future reconfigurable digital coherent systems without inline dispersion compensation, the transmission distance may be obtained from network management systems from upper layer protocols. In case this is not available, one can look at the accumulated CD that can be read out from the filter taps of the DSP-based CD compensation filter. Assume that the fiber type is homogenous across the network (which is reasonable but of course not always true), the digital coherent receiver is able to provide a rough estimate of the link transmission distance. In any case, according to Fig. 2.7 and Fig. 2.9, it can be deducted that with a large distance estimation error up to 100 km, the corresponding ξ (obtained from look-up table) will deviate by at most 0.3 dB from the optimal value, which translates into another

0.2 dB OSNR estimation error for PM-QPSK systems and 0.4 dB for PM-16-QAM systems. Therefore, our technique is rather insensitive to inaccurate estimation of transmission distance.

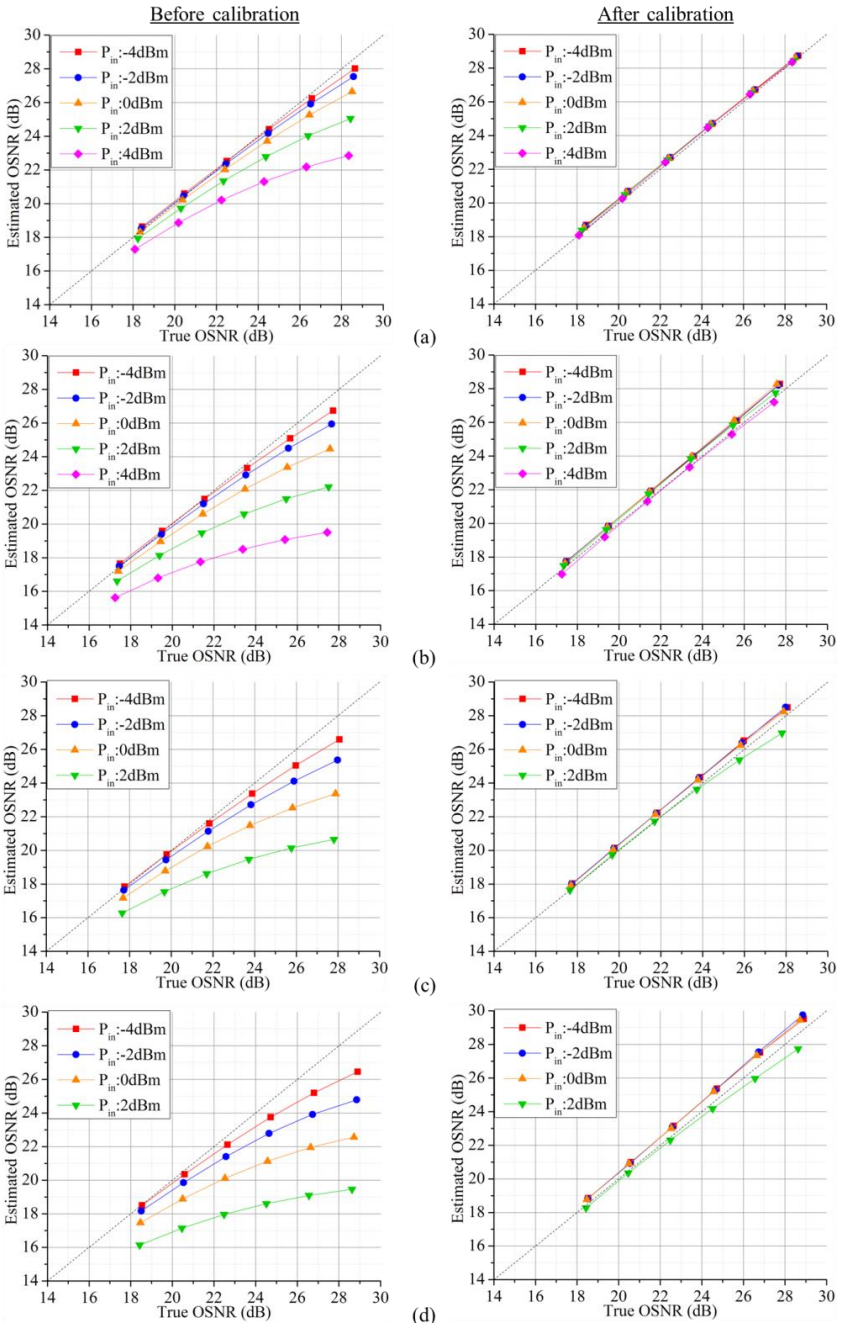

Fig. 2.8. Estimated OSNR vs true OSNR for a 224 Gb/s PM-16-QAM system obtained from simulations for various signal launched powers and OSNR values (a) after 400km transmission and calibrated with ξ=11.2. The maximum estimation error is 0.9 dB; (b) after 800 km transmission and calibrated with ξ=12.3. The maximum estimation error is 1.73 dB; (c) after 1200 km transmission calibrated with ξ=12.8. The maximum estimation

error is 1.81 dB; (d) after 1600 km transmission calibrated with ξ=13.8. The maximum estimation error is 1.98 dB. Different pulse shapes, timing phases, PDL and DGD with different SOPs are considered in the simulation and estimation results.

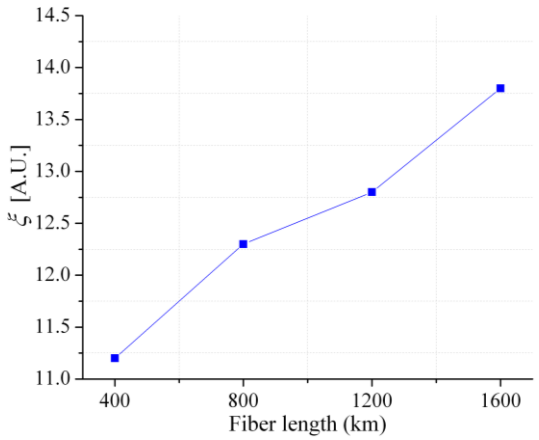

Fig. 2.9. The optimized calibration factor ξ vs. transmission distance for a 224 Gb/s PM-16-QAM system for realizing nonlinearity-insensitive OSNR monitoring.

In addition, we briefly investigated the performance of the proposed OSNR monitoring technique in WDM systems. In the presence of inter-channel nonlinear effects such as XPM and FWM, the signals are further degraded by the additional nonlinear distortions. However, those additional nonlinear distortions can be calibrated into our EVM-based OSNR estimator using a larger ξ. The optimized ξ versus transmission distance for a multi-channel 224 Gb/s PM-16-QAM system with 50 GHz channel spacing is show in Fig. 2.10. We can see that with inter-channel nonlinear impairments the optimal ξ increases with the number of channels and saturates when the number of channels exceeds 9. This is in agreement with expectations as channels spaced far apart interacts less with each other through XPM due to walk-off effects. For a 21-channel WDM system, the maximum monitoring errors are 0.8 dB, 1.1 dB, 1.5 dB and 2.2 dB for 400 km, 800 km, 1200 km and 1600 km transmissions respectively.

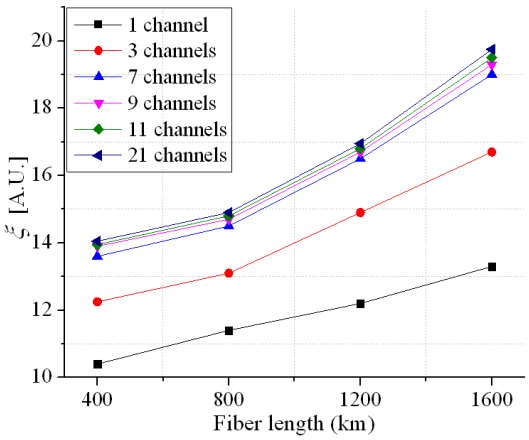

Fig. 2.10. The optimized calibration factor ξ vs. transmission distance for a 224 Gb/s PM-16-QAM WDM system for realizing nonlinearity-insensitive OSNR monitoring. The channel spacing is 50 GHz.

2.4. Summary

In this chapter, we proposed a fiber-nonlinearity-insensitive OSNR monitoring technique for digital coherent receivers by incorporating and calibrating fiber nonlinearity-induced amplitude noise correlations among neighboring symbols into conventional OSNR estimation techniques from received signal distributions. For 112Gb/s PM-QPSK systems, accurate OSNR monitoring in the range of 10–24 dB is experimentally demonstrated by the proposed technique in presence of relatively strong fiber nonlinearity. For 224 Gb/s PM-16-QAM systems, simulation results demonstrated accurate OSNR monitoring in the range of 18-28 dB and the proposed OSNR monitoring technique is shown to be robust against different signal pulse shapes, timing phase offsets, PDL and first-order PMD effects. Finally, studies on multi-channel 224 Gb/s PM-16-QAM WDM systems demonstrated the validity of the proposed OSNR monitoring technique in the presence of inter-channel nonlinearities. Further investigations on the proposed methodology to estimate the OSNR accurately without the prior knowledge of the system configurations such as the transmission distance and number of WDM channels will be attempted in the future. This can result in a nonlinearity-insensitive OSNR monitoring technique that is applicable in dynamic and flexible network environments, which may hold key to its commercial implementation in software defined networks.

Chapter 3

OSNR Monitoring insensitive to Cascaded Filtering Effects by Low-cost Coherent Receptions and RF Power Measurements

3.1. Introduction

Fiber-optic communication networks are evolving to employ adaptive modulation formats and complex network architectures utilizing reconfigurable optical add/drop multiplexers (ROADMs) to promote flexibility, dynamicity and better utilization of available transmission capacity [62]. OSNR monitoring are indispensable for such complex networks as they can provide failure diagnosis, optimization and real-time performance monitoring for dynamic lightpath provisioning and modulation format adaptation. So far, in-band OSNR monitoring can be easily realized at the receiver from the statistical moments or the distributions of equalized signals by relatively simple algorithms [26]-[30] and such OPM functionality is essentially a by-product of the digital coherent receiver. However, OSNR monitors need to be deployed ubiquitously across the network including intermediate nodes where coherent receiver solutions are simply too costly and impractical. Consequently, a reliable, low-cost, modulation-format-independent OSNR monitor for distributed monitoring of optical networks is in demand. In [31], a data-aided OSNR estimation technique utilizes Golay sequences as its training symbols and obtains the OSNR from the variance of the power spectrum of Golay sequences as it is proportional to the expected value of noise power spectral density. The method only utilizes a low-bandwidth coherent receiver working at low sampling rate and is modulation-format-independent but requires the modification of transmitters. Another monitoring technique [63] proposed the use of an optical delay interferometer (ODI), by measuring the optical power of the constructive and destructive output ports using simple, low-speed photodiodes, to determine the power associated with the signal and the noise and thus determine the OSNR. However, the impact of spectral narrowing by cascaded WSSs limits the monitoring accuracy because the spectral shape needs to be constant along transmission. Recently, an OSNR monitoring method using tunable optical band pass filter with optical

power measurements was reported in [64][65]. However, the monitoring accuracy relies on the bandwidth of the optical filter and a very narrow bandwidth (several GHz, expensive and not commercially available at present) is needed to guarantee a good monitoring accuracy [64]. Besides, it may also suffer from WSS induced spectral narrowing.

In this chapter, we propose a low-cost and modulation-format-independent OSNR monitor utilizing reduced-complexity coherent receptions, electrical filtering and RF power measurements. By measuring the RF power of three different frequency components of the coherently received baseband signals, the proposed technique is also insensitive to spectral narrowing by WSSs. We experimentally demonstrate accurate (<0.7 dB error) OSNR monitoring for various modulation formats and transmission distances, hence different number of WSSs. We also study the robustness of the proposed technique to the fiber nonlinearity, laser effects in a five-channel WDM system at 50-GHz spacing and other practical considerations.

3.2. Principle of Proposed In-band OSNR Monitor

Fig. 3.1 shows the schematic diagram of the proposed in-band OSNR monitor as the key function of an OPM that can be deployed in different locations across an optical network. It consists of a tunable laser that functions as a LO, a 3dB coupler, a low-speed balanced detector (several GHz), a low-pass electrical filter, an RF power meter and a control and process unit (CPU). The incoming optical signals tapped from the transmission link firstly go into a 3dB coupler, where the signals interfered with the light of tunable laser. Since no phase or polarization information is required for the monitoring, a 3 dB coupler rather than a polarization diversity optical quadrature front-end (2×4 90° hybrid) is used to coherently receive the signals. After balance detection, the resulting baseband RF signals then go into an electrical low-pass filter. By tuning the frequency of the tunable laser to the center frequency f_{CF} and an offset frequency f_{OF1} of the target optical signal, the signal components around f_{CF} and f_{OF1} falls into the passband of the electrical filter and are measured by the RF power meter as P_{CF} and P_{OF1} respectively (See Fig. 3.1(b)). Here the tunable laser does not only act as a frequency selector, but, as an additional advantage, amplify the signal to a proper level to avoid the detrimental effects of electronic thermal noise on the accuracy of the proposed OSNR monitoring technique. Also it should be noted that the

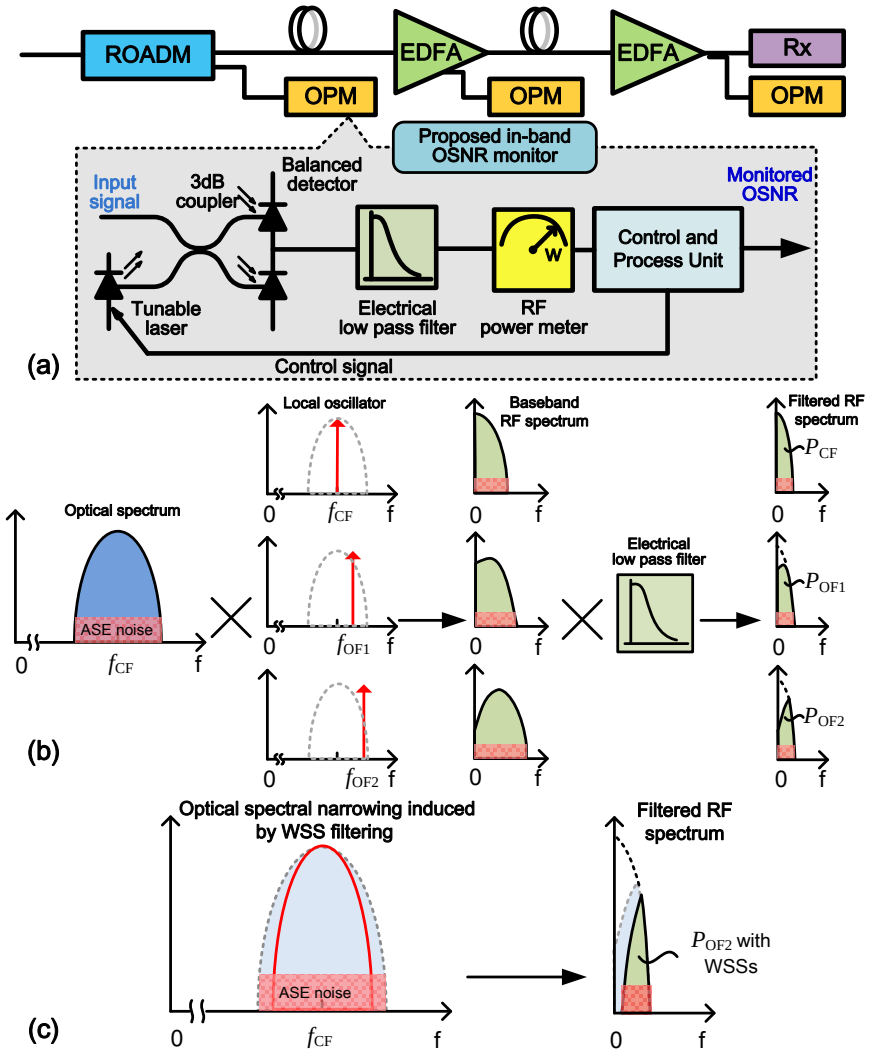

Fig. 3.1. (a) Schematic diagram of proposed OSNR monitor; (b) Signal spectra before and after coherent receptions; RF spectrum after electrical filtering showing filtered signal (marked in green) and ASE noise (marked in red), whereas P_{CF}, P_{OF1} and P_{OF2} denote RF power after electrical filtering when the LO frequency is set to the center frequency of the spectrum f_{CF} and two other offset frequencies f_{OF1} and f_{OF2}, (c) WSS filtering induced optical spectral narrowing and RF spectral narrowing. ROADM: reconfigurable optical add-drop multiplexer, EDFA: erbium-doped fiber amplifier, OPM: optical performance monitor, Rx: receiver. ASE: amplified spontaneous emission.

devices used in our proposed monitor such as the 3dB coupler, the tunable laser with a linwidth of few MHz, balanced detector with several GHz bandwidth and the electrical low-pass filter are all commercially available and low-cost.

In coherent receivers, for sufficiently high LO powers, ASE noise is usually dominant and other noise components like shot-noise and thermal noise can be neglected. Since the ASE noise can be modeled as AWGN, its power P_{ASE} around frequencies f_{CF} and f_{OF1} within a given band are assumed to be the same, while the signal power P_{SIG} within the two bands are determined by the signal pulse shape which normally are not the same. The relationship between P_{CF}, P_{OF1}, P_{SIG} and P_{ASE} can be described as [64]

$$P_{CF} = P_{SIG} + P_{ASE}, \qquad P_{OF1} = R_1 P_{SIG} + P_{ASE}. \tag{2.7}$$

The calibration parameter R_1 can be obtained by placing the monitor at the transmitter (Tx) side and performing a back-to-back measurement where the ASE noise is negligible, i.e. $R_1=P_{OF1\text{-}Tx}/P_{CF\text{-}Tx}$. The OSNR can then be calculated by the CPU as

$$OSNR = \gamma \frac{P_{SIG}}{P_{ASE}} = \gamma \frac{1 - P_{CF}/P_{OF1}}{(P_{CF}/P_{OF1})R_1 - 1}, \tag{2.8}$$

where the calibration parameter γ is determined by the electrical filter bandwidth and signal bandwidth.

It should be noted that the calibration parameter R_1 depends on the signal spectral shape and remain unchanged only when there is no additional filtering effect. However, WSSs in ROADMs are essential parts of present optical networks and cascaded filtering effects by WSSs during signal transmission are known to affect spectral shapes. Fig. 3.1(c) shows the spectral narrowing effect for a 25-Gbaud signal by cascaded WSSs. The shape of the sideband is obviously changed and thus the relationship in (2.7) will no longer hold which may lead to unacceptable OSNR monitoring errors. In order to cope with spectral narrowing in the OSNR monitoring, we can take another RF power measurement P_{OF2} at a second offset frequency f_{OF2} (See Fig. 3.1(b)) and define a calibration parameter R_2 similar to R_1. Additionally, two more parameters α and β are defined to characterize the effect of a WSS on the spectral shape at f_{OF1} and f_{OF2} respectively, which can be obtained by placing a WSS between the transmitter and the monitor and performing a back-to-back measurement, or by verified theoretical models of WSS filter shapes [66]. In the presence of N cascaded WSSs in the transmission link, the measured power can be re-written as

$$P_{CF} = P_{SIG} + P_{ASE}, \qquad P_{OF1} = R_1 \alpha^N P_{SIG} + P_{ASE}, \qquad P_{OF2} = R_2 \beta^N P_{SIG} + P_{ASE}. \tag{2.9}$$

By solving the three equations above, we can obtain N, P_{SIG} and P_{ASE} and thus calculate the OSNR by the implicit equation

$$\frac{P_{OF1}}{P_{CF} R_1} + \frac{P_{OF1}/P_{CF} - 1}{R_1 \cdot OSNR} = \left(\frac{P_{OF2}}{P_{CF} R_2} + \frac{P_{OF2}/P_{CF} - 1}{R_2 \cdot OSNR} \right)^{\log \alpha / \log \beta}. \tag{2.10}$$

3.3. Experimental and Simulation results

3.3.1. Experimental Setup and Results

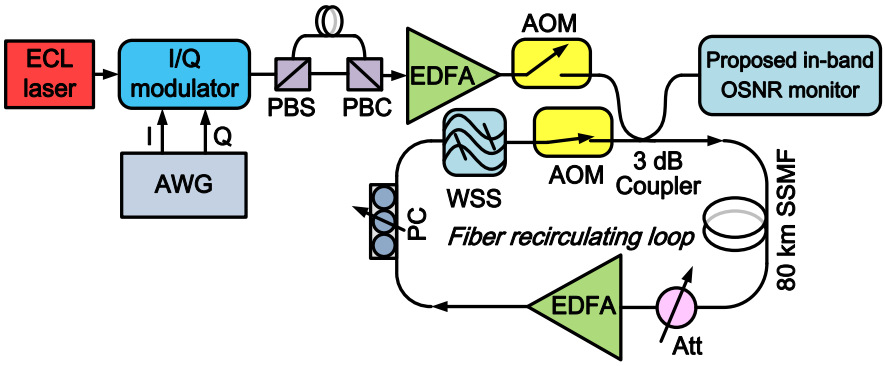

Fig. 3.2. Experimental setup. Att: attenuator, AWG: arbitrary waveform generator, AOM: acousto-optic modulator, ECL: external cavity laser, PBS: polarization beam splitter, PBC: polarizing beam combiner, PC: polarization controller, SSMF: standard single-mode fiber.

Fig. 3.2 shows the experimental setup used to evaluate the performance of the proposed monitoring technique. At the transmitter side, an ECL sends a continuous-wave (CW) light with 100 kHz linewidth at 1553.12 nm and is modulated using an I/Q modulator, of which the I and Q branches are driven independently by two uncorrelated 25-Gbaud PRBSs (length=2^{15}-1) produced by the arbitrary waveform generator (AWG). In order to verify the transparence of the proposed technique to various modulation formats, we generate three common signals, DP-QPSK, DP-16-QAM and DP-64-QAM, by modulate the I/Q modulator with 2-level, 4-level and 8-level pulse-amplitude modulation (PAM) electrical signals, respectively. Polarization division multiplexing is achieved by splitting the signal through a PBS into two branches, delaying one branch, and recombining the signal through a

PBC. The signal is then amplified to around 0 dBm and launched into a fiber recirculating loop, which consists of a span of 80 km SSMF, an EDFA and a programmable WSS. The EDFA fully compensates the total loss in the loop. A tunable attenuator is placed before the EDFA to realize various OSNR values for the received signals. The WSS is set to 50-GHz bandwidth with 5th-order super-Gaussian shape and with an all-pass shape for the two neighbouring channels as shown in Fig. 3.3. As a result, the out-band noise is preserved in the neighbouring channels even through the signal undergo cascaded filtering effects. At the loop output, the OSNR values of the received signals are measured by the proposed monitor which are then compared with the reference OSNR measured by an OSA using out-of-band noise measurement [57] referring to 0.1 nm noise bandwidth. The RF power meter used in the experiments has a sensitivity of as low as -60 dBm and a frequency range from 10 MHz to 18 GHz. However, since the power meter cannot be triggered fast enough to measure the signals coming from the recirculating loop, we only use it to perform the back to back experiment. For those transmission experiments requiring fiber recirculating loop, a 80-Gsamples/s real-time oscilloscope is used instead of the RF power meter to measure the RF signal powers in the following steps: 1) Capturing a sequence (length=400000) of the signals from the balanced detector, 2) filtering the signals with a digital low pass filter and 3) calculating the power of the signals. We again note that such real-time scope for RF power measurement is not required in realistic optical networks with straight-line links.

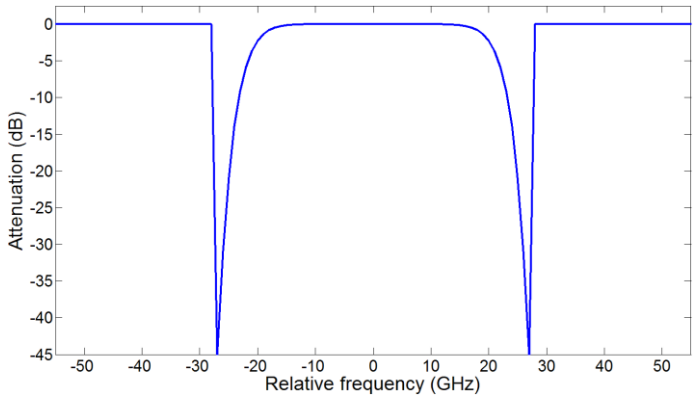

Fig. 3.3. Amplitude spectrum of the programmable WSS with 5th-order super-Gaussian transfer function for the channel of interest and all-pass shapes for the two neighboring channels.

The design parameters for the OSNR monitor include the bandwidth of the electrical low-pass filter and the offset frequency f_{OF1} and f_{OF2}, which determine the proposed monitoring accuracy [64].

Fig. 3.4 shows the experimental results for the accuracy of the OSNR monitor of DP-64-QAM signals transmitted over 640 km by changing the bandwidth of the digital low-pass filter from 500 MHz to 8 GHz, whereas the f_{OF1} and f_{OF2} are fixed at f_{CF}+20 GHz and f_{CF}+23.5 GHz respectively. As expected, the filter with lowest bandwidth (500 MHz) resulted in the minimum error which is less than 0.2 dB, and the error level increases as the bandwidth increases. The maximum error will be larger than 1dB when the bandwidth is set to be larger than 6 GHz. Since a negligible error level increment of 0.1 dB occurs when the bandwidth increases from 500 MHz to 800 MHz, we choose the bandwidth of the low-pass filter to be 800 MHz for the rest of the chapter so as to relax the sensitivity requirement of the RF power meter.

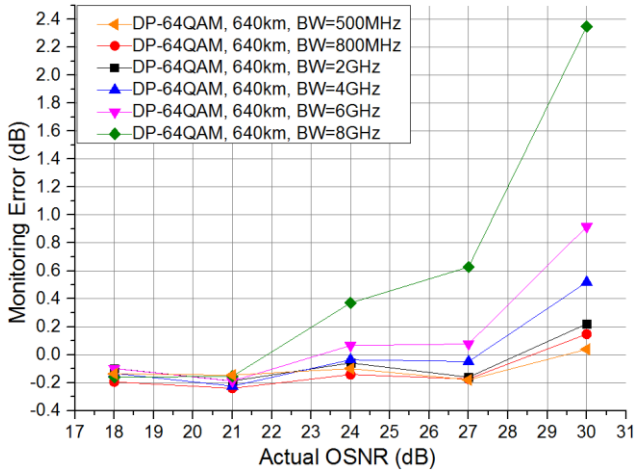

Fig. 3.4. Experimental OSNR monitoring error versus actual OSNR for DP-64-QAM signals transmitted over 640 km using an electrical filter with bandwidth from 500 MHz to 8GHz.

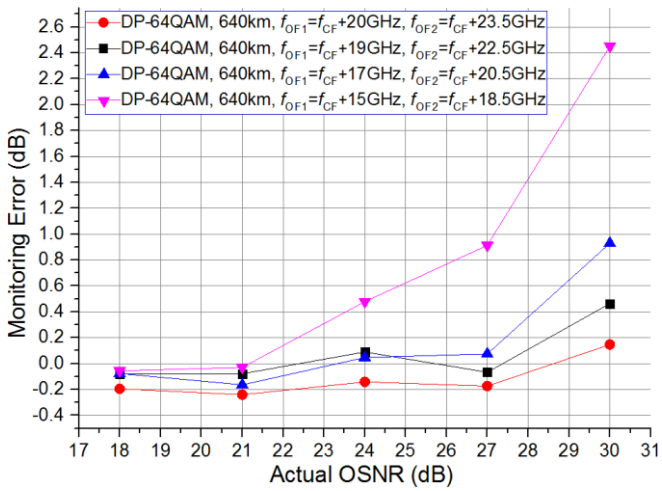

Fig. 3.5. Experimental OSNR monitoring error versus actual OSNR for DP-64-QAM signals transmitted over 640 km using various sets of offset frequency f_{OF1} and f_{OF2}.

Fig. 3.5 shows the accuracy of the proposed OSNR monitoring scheme for DP-64-QAM signals transmitted over 640 km at different sets of f_{OF1} and f_{OF2}, whereas the frequency difference between f_{OF1} and f_{OF2} is fixed at 3.5 GHz. As shown, an error of larger than 1 dB occurs when the f_{OF1} and f_{OF2} are set at f_{CF}+15 GHz and f_{CF}+18.5 GHz respectively. As the offset frequencies are set closer to the edge of the signal spectrum, the error level decreases and a minimum error level of <0.3 dB is achieved by setting f_{OF1} and f_{OF2} at f_{CF}+20 GHz and f_{CF}+23.5 GHz respectively. We shall not further set f_{OF1} and f_{OF2} closer to the edge of the spectrum since in a WDM system overlaps of the neighboring channels may occur and a proper guard band (i.e., >1.5 GHz) between f_{OF2} and the edge frequency should be guaranteed.

In order to demonstrate the data-format independence and the insensitivity to filtering effects of the proposed monitor, we perform experiments for different modulation formats and different distance, i.e. different number of WSSs. To achieve best monitoring accuracy, we choose the electrical filter with a bandwidth of 800 MHz and set the offset frequencies f_{OF1} and f_{OF2} to be 20 GHz and 23.5 GHz respectively. It should be noted that we replace the digital low-pass filter by an analog filter to realize the experimental setup in a more practical way. For DP-QPSK and DP-16-QAM signals, experiments of 640 km and 1280 km transmission are performed. For DP-64-QAM signal, experiments of back-to-back (BTB), 320 km and 640 km transmission are performed. We use the same sets of calibration parameters R_1, R_2, α and β determined by taking a back-to-back measurement using DP-16-QAM

signals for all the OSNR calculations of different modulation formats and transmission distances. Each monitoring error is taken from the average of 8 independent measurements.

As shown in Fig. 3.6, for DP-64-QAM signals, the OSNR monitor achieved <0.6 dB accuracy for OSNR values from 18 to 30 dB and a transmission distance up to 640 km (8 WSSs), whereas for DP-16-QAM and DP-QPSK signals, monitoring error is less than 0.7 dB for OSNR values from 12 to 27 dB and a transmission distance up to 1280 km (16 WSSs). The accuracy of the monitoring results across different modulation formats and distances show that the OSNR monitor can perform accurately independent of the data format and insensitive to the WSS filtering. On the other hand, note that if we only use (2.8) to calculate the OSNR for DP-64-QAM signals after 640 km transmission i.e. 8 cascaded WSS filters, the maximum monitoring error can be larger than 5 dB (represented by the pink curve in Fig. 3.6). Therefore, incorporating P_{OF2} and some prior knowledge of the WSS filter shape in the OSNR monitoring is pivotal to its robustness against cascaded filtering effects.

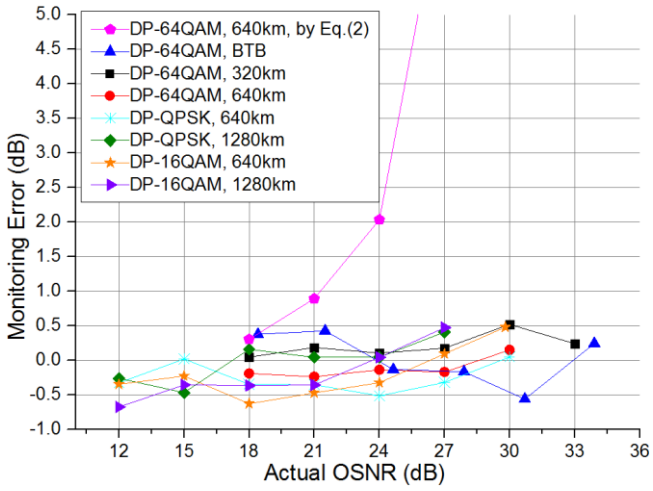

Fig. 3.6. Experimental OSNR monitoring error versus actual OSNR for DP-QPSK/16-QAM /64-QAM signals over various transmission distances (different number of WSSs). All the monitoring errors are less than 0.7 dB by using Eq. (4). The results showed in pink curve are the monitoring errors for DP-64-QAM signals after 640 km transmission obtained by using (2.8) when WSS filtering is not taken into account.

Since no frequency-locked loop (FLL) is used in the proposed monitor, frequency offset (FO) between the transmitter and receiver lasers will exist in practical applications. Fig. 3.7 shows the OSNR monitoring errors for DP-64-QAM signals transmitted over 640 km with various amounts of

intentionally introduced FO. As shown in the figure, the monitoring error increases with FO but a <0.9 dB monitoring error for FO up to 1 GHz for OSNR below 30 dB can still be maintained. Recently, a low-cost, fast-tuning MGY semiconductor laser co-packaged with a frequency-referencing etalon with < 0.5 GHz accuracy was demonstrated in [67] and can be used in our proposed monitor for accurate frequency tracking. Alternatively, one can identify the frequency that gives the largest P_{CF} in the electrical spectrum as the center frequency f_{CF} and carry out the calculations in (2.10). In that case, the absolute frequency offsets are no longer a detrimental factor and the monitoring accuracy are more robust to laser frequency offsets.

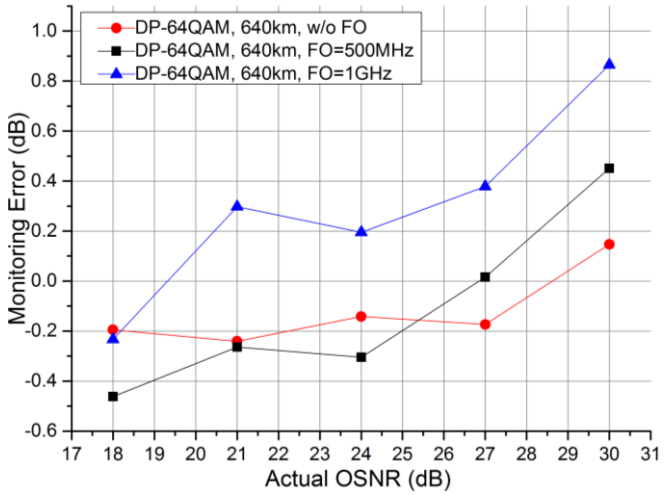

Fig. 3.7. Experimental OSNR monitoring error versus actual OSNR for DP-64-QAM signals transmitted over 640 km in the presence of different frequency offsets up to 1 GHz between the lasers of transmitter and receiver.

3.3.2. Robustness of the Proposed OSNR Monitoring Technique to Fiber Nonlinearities, Laser Effects in WDM Systems and Other Practical Considerations

We conduct simulations using VPI [58] to investigate the influence of nonlinear effects in a WDM system on the accuracy of the proposed OSNR monitor. We perform WDM transmissions using five-channel 25-Gbaud DP-16-QAM and DP-64-QAM signals with 50-GHz channel spacing over 640 km fiber. The wavelength multiplexer at the transmitter end has 50-GHz bandwidth with 4th-order super-Gaussian shape. The remaining part of the system setup is the same as that shown in Fig. 3.2 and the

bandwidth of the electrical filter, the offset frequencies f_{OF1} and f_{OF2} are chosen to be 800 MHz, 20 GHz and 23.5 GHz respectively, the same as those in the experiments.

Fig. 3.8 shows the measured OSNR versus the actual OSNR for the DP-16-QAM and DP-64-QAM signals at 0 dBm and 4 dBm launched power per channel at the center channel (CH3) and at the edge channel (CH1) of a five-channel WDM system with 50-GHz ITU grid. In the presence of weak nonlinearities (0 dBm/channel), for OSNR values of <30 dB, the OSNR monitor achieves <0.4 dB accuracy for both the edge channel and the center channel for both modulation formats. The monitoring error of the edge channel CH1 is a little bit larger than that of center channel CH3 as the calibration parameters R_1, R_2, α and β used for the OSNR calculation of CH1 are obtained from CH3 and the true calibration parameters may slightly vary among different channels. However, the similarity of the depicted curves for different WDM channels verifies the wavelength independency of the proposed monitoring technique. As the launched power increases to 4 dBm per channel, some nonlinearity is present and the monitoring accuracy is reduced due to the nonlinearity-induced spectrum broadening. It can be seen that the monitoring accuracy of center channel suffers more nonlinearities than the edge channel since the center channel is more vulnerable to cross phase modulation effects. However, the error levels of both channels and both modulation formats are still less than 1 dB which indicate that the proposed method can work properly in the presence of moderate amount of nonlinearity.

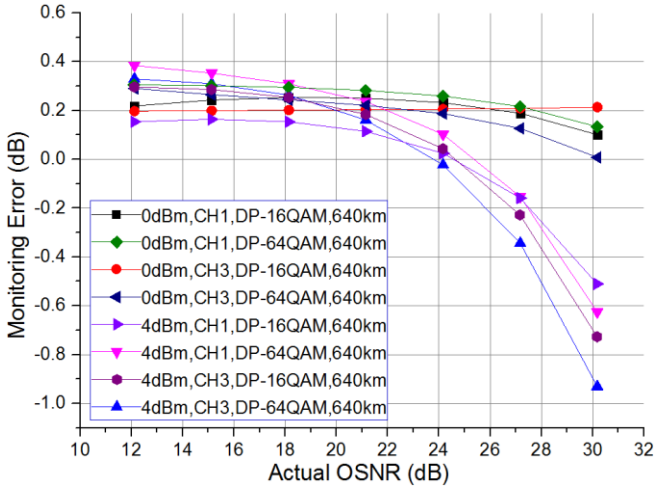

Fig. 3.8. Simulated OSNR monitoring error versus actual OSNR for DP-16-QAM and DP-64-QAM signals transmitted over 640 km of different channels in a WDM system at different launched power per channel.

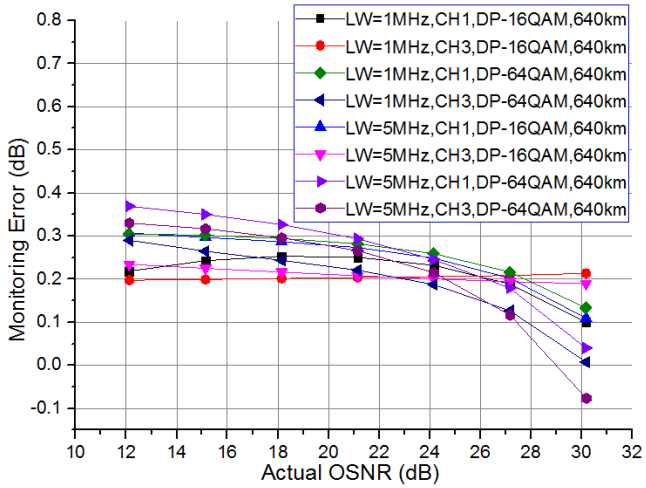

Fig. 3.9. Simulated OSNR monitoring error versus actual OSNR for DP-16-QAM and DP-64-QAM signals transmitted over 640 km of different channels in a WDM system using LO with 1-MHz and 5-MHz linewidth.

We also investigate the influence of the linewidth of the tunable laser on the accuracy of the proposed OSNR monitor in the WDM system. In order to realize the monitor in a low-cost fashion, the tunable laser used inside the monitor as the LO is preferred to be realized by a DFB laser with a typical linewidth (LW) of several MHz. Fig. 3.9 compares the performance of the OSNR monitor using the LO with a linewidth of 1 MHz and 5 MHz for DP-16-QAM and DP-64-QAM signals of both edge channel and center channel. It can be seen from the figure that the error levels increase only very slightly with the linewidth of both channels and modulation formats. The maximum error increases by 0.2 dB as the linewidth increases from 1 MHz to 5 MHz and the maximum error of both channels and modulation formats are still less than 0.4 dB.

In addition, the calibration parameters R_1, R_2, α and β used for all the OSNR calculations are determined by taking a back-to-back measurement using DP-16-QAM signals at the center channel. It should be noted that R_1, R_2 depends on the signal spectral shape and α, β depends on the WSS shape at f_{OF1} and f_{OF2} and these calibration parameters may vary with the constituent devices in practice, which in turn may affect the OSNR monitoring accuracy. We performed simulations to monitor the OSNR of received DP-QPSK signals after 800 km transmission through 10 WSSs to investigate the impact of the calibration parameters mismatch on the monitoring error and the results are shown in Fig. 3.10. When these 4 parameters are off by less than 8% of their actual values, the monitoring errors can still

be kept under 1 dB. On the other hand, note that the estimated number of cascaded WSSs *N* (shown in the legend), deviates from its actual value 10 considerably. Fortunately, that is of little concern for our overall objective of accurate OSNR monitoring.

Further to calibration parameter mismatches, the center frequencies, bandwidths and even the shapes of WSS may vary slightly from channel to channel and from device to device in practice, which in turn can affect the accuracy of the proposed OSNR monitoring scheme. We performed simulations for DP-QPSK transmissions over 800 km with non-identical WSSs and the results are shown in Fig. 3.11. The 10 WSSs are assigned with different center frequency, bandwidth and the order of super-Gaussian shape. In case 1, all the 10 WSSs are identical and well-aligned without any frequency shift. The bandwidth and order of super-Gaussian function of each WSS are 50 GHz and 4, respectively. In the 'interleaved' case 2 and case 3 [68], the center frequency shift is -2 and -3 GHz for about half the WSSs and +2 and +3 GHz for the remaining WSSs, respectively. In the 'unidirectional' case 4 and case 5, all the WSSs have the same center frequency shift of +3 and -3 GHz, respectively. In the case 6 and case 7, all the WSSs have the same bandwidth of 47 GHz and 53 GHz, respectively. In the case 8 and case 9, all the WSSs have the same 3^{rd}-order super-Gaussian shape and 5^{th}-order super-Gaussian shape, respectively. In the case number 10, all the 10 WSSs are not identical and are randomly picked from cases 1-9. As can be seen from Fig. 3.11, the estimated *N* (shown in the legend with *N*=10 as correct value) is very sensitive to such WSS parameter variations. For the OSNR estimates, the worst case scenario occurs when all the WSSs have a +3 GHz frequency shift (case 4) and the largest error is nearly 0.9 dB i.e. a <1 dB monitoring error can be obtained when the cascaded WSSs are not identical. It seems that the overall effect of spectrum narrowing of cascaded WSSs with different center frequencies, bandwidths and shapes will mostly affect the accuracy of the estimated number of WSS *N* while the accuracy of the estimated OSNR is less sensitive to such variations and perturbations.

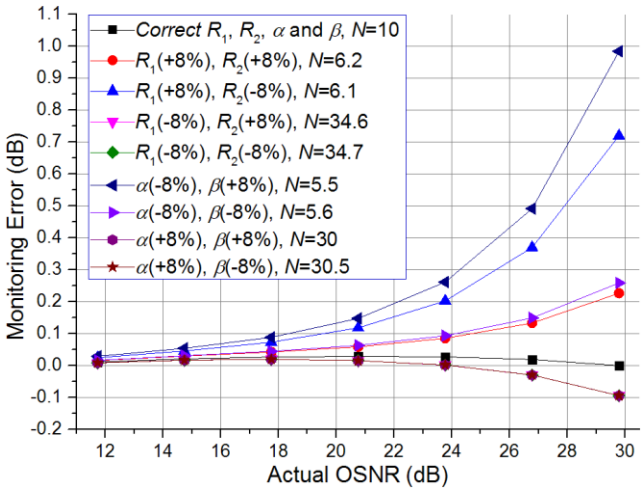

Fig. 3.10. Simulated OSNR monitoring error versus actual OSNR for DP-QPSK signals transmitted over 800 km under different degrees of calibration parameter mismatches.

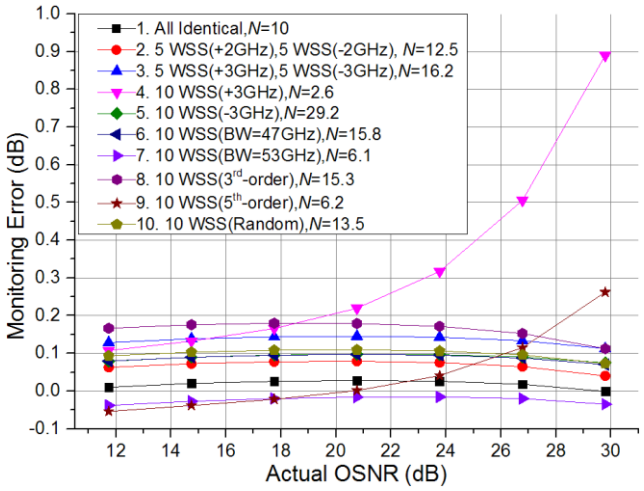

Fig. 3.11. OSNR monitoring error versus actual OSNR for DP-QPSK signals transmitted over 800 km with non-identical cascaded WSSs.

3.4. Summary

In this chapter, we proposed and demonstrated a low-cost, modulation-format-independent OSNR monitoring scheme using a low-cost and reduced-complexity coherent receiver, simple electrical filtering and RF power measurements. By measuring and processing the RF power of three different frequency components of the coherently received baseband signals, the proposed OSNR monitor is also insensitive to spectral narrowing effects induced by cascaded WSSs. We experimentally studied OSNR

monitoring for 25-Gbaud DP-QPSK, DP-16-QAM and DP-64-QAM signals transmitted over various distance (hence different number of WSSs) and demonstrated accurate OSNR monitoring across a wide range of system conditions. In addition, we investigated the influence of different parameters, including the bandwidth of the electrical low-pass filter, the laser frequency offset and laser linewidth on the monitoring accuracy. The proposed technique is also shown to be robust to the fiber nonlinearities, calibration parameter mismatches and random variations of WSS parameters within a certain range. However, it should be noted that the proposed scheme relies on the prior knowledge of the pulse shape and the WSS spectral shape and hence some calibration might be necessary in practice before the operation of the proposed OSNR monitoring technique.

Chapter 4

Nonlinear Frequency Division Multiplexed Transmissions based on Nonlinear Fourier Transform

4.1. Introduction

Kerr nonlinearity is always believed to be a fundamental capacity-limiting factor in fiber-optic communications. Soliton transmissions were extensively investigated in the 1990s as a promising technology for data transmission over the nonlinear fiber-optic channel, but EDFA and WDM technologies evolved as more practical system upgrades. Advances made over the past decade in coherent detection and DSP have significantly improved transmission capacities to a point where nonlinearity once again becomes the limiting factor [69] even with advanced modulation formats, error-control coding and arbitrarily complex DSP. Nonlinearity compensation algorithms such as digital back-propagation [33][37] have been proposed to partially combat fiber nonlinearities but the performance gain is severely limited by noise-nonlinearity interactions and XPM effects. The recently revived NFDM systems based on the theoretical framework of NFT is proposed as a new signaling scheme that incorporates soliton theory with communication theory [42]-[44]. NFDM resembles the commonly-known OFDM philosophy in that independent information streams are encoded in parallel sub-carriers (eigenvalues of the Lax operator governing the nonlinear propagation) that are analytically shown to be independent of each other upon propagation in an ideal noiseless and lossless fiber channel. In principle, NFDM is also largely immune to XPM effects and thus it has gained recent attention as a potential fundamental breakthrough for communications over the nonlinear fiber channel. Several preliminary works were conducted including regular BPSK signal transmission with receiver NFT processing [70], eigenvalues transmission with direct detection [71], simulation studies for eigenvalue multiplexing transmission [72], experimental characterization of noise tolerance of back-to-back eigenvalue transmissions with NFT processing [73] and numerical studies of OFDM transmissions using NFT mapping of the continuous spectrum at the transmitter and NFT receiver processing [74]. Most recently, independent QPSK modulation on 2 eigenvalues is reported [75].

In this chapter, we focus on the study of NFDM systems based on the OOK modulation of discrete spectrum. We, for the first time, experimentally demonstrate successful simultaneous and independent modulation and transmission of 3-eigenvalue multisoliton NFDM signals. The signal set consists of 1-, 2-, 3-solitons and their various nonlinear combinations. Error-free transmission over an 1800 km link of standard single-mode fiber with Raman amplification and coherent detection is demonstrated. Extensions to 4-eigenvalue transmissions are also experimentally investigated. Furthermore, we study the impact of frequency offset and laser phase noise such OOK modulated NFDM systems. Simulation results show that they are robust to the frequency offset and laser phase noise in a certain range.

4.2. Nonlinear Fourier Transform

The key idea of NFT is to seek an operator *L(q)* whose spectrum (eigenvalues) remains constant even as signal *q(t,z)* evolves in z according to some evolution equation $q_z=K(q)$. If the spectrum of *L(q)* do not depend on z, then we refer to *L(q)* as an isospectral family of operators (as shown in Fig. 4.1). Let *L(q)* be a diagonalizable family of operators. Then *L(z)* is an isospectral family if and only if it satisfies

$$L_z = \frac{dL}{dz} = ML - LM = [M, L], \tag{3.1}$$

for some operator *M(q)* [42]. The operators *L(q)* and *M(q)* satisfying (3.1) are called a *Lax Pair* [76].

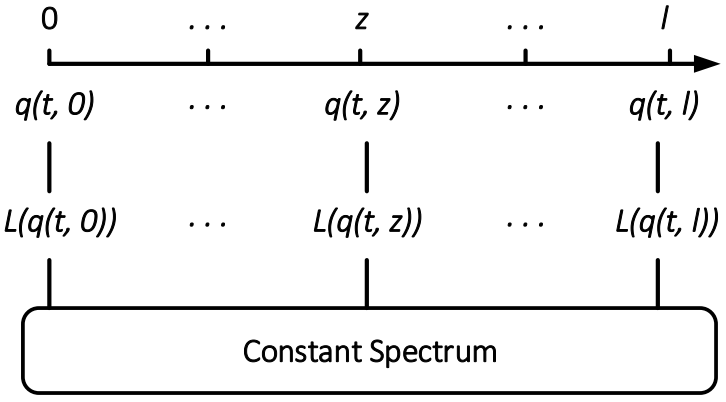

Fig. 4.1. An isospectral flow: the spectrum of *L* is held invariant even as *q*(*t*, *z*) evolves [42].

As the optical waveform *q(t,z)* propagating in fiber links varies based on the NLS equation (1.1), according to the Zakharov-Shabat system [77], if we choose *L(q)* and *M(q)* as

$$L = j\begin{pmatrix} \dfrac{\partial}{\partial t} & -q(t,z) \\ -q(t,z) & -\dfrac{\partial}{\partial t} \end{pmatrix}, \qquad M = j\begin{pmatrix} 2j\lambda^2 - j\left|q(t,z)\right|^2 & -2\lambda q(t,z) - jq_t(t,z) \\ 2\lambda q^*(t,z) - jq_t^*(t,z) & -2j\lambda^2 + j\left|q(t,z)\right|^2 \end{pmatrix},$$

(3.2)

then the eigenvalues of *L(q)* are constant during the evolution in an isospectral flow, which are defined via

$$Lv = \lambda v, \tag{3.3}$$

where λ and v are, respectively, the eigenvalue and eigenvector. Taking the *z* derivative of (3.3) and using the Lax equation $L_z = [M, L]$, it shows that an eigenvector of *L* evolves according to the linear equation

$$v_z = Mv. \tag{3.4}$$

Additionally, we can re-write Eq. (3.3) as

$$v_t = Pv. \tag{3.5}$$

where the operator *P* is the Zakharov-Shabat system and is given by

$$P = \begin{pmatrix} -j\lambda & q(t,z) \\ -q^*(t,z) & j\lambda \end{pmatrix} v, \tag{3.6}$$

The NFT of a signal $q(t)$, supported in the interval $[T_1,T_2]$, can be obtained by solving the differential system (3.5) with

$$v(T_1,\lambda) = \begin{pmatrix} 1 \\ 0 \end{pmatrix} e^{-j\lambda T_1}, \tag{3.7}$$

Let the time-independent complex-scalar nonlinear Fourier coefficients *a(λ), b(λ)* to be

$$a(\lambda) = v_1(T_2,\lambda)e^{j\lambda T_2}, \tag{3.8}$$

and

$$b(\lambda) = v_2(T_2,\lambda)e^{j\lambda T_2}, \tag{3.9}$$

then the NFT of $q(t)$ with respect to the Lax operator *L* as a function of the complex-valued frequencies λ consists of two types of spectral functions [42]:

$$\tilde{q}(\lambda_j) = \frac{b(\lambda_j)}{a'(\lambda_j)}, \lambda_j \in S \subset \mathbb{C}^+, j = 1,2,3...,N, \tag{3.10}$$

$$q(\lambda) = \frac{b(\lambda)}{a(\lambda)}, \lambda \in \mathbb{R} \tag{3.11}$$

where $\tilde{q}(\lambda_j)$ is the discrete (or point) spectrum which occurs in the upper half complex plane $\mathbb{C}^+$ and corresponds to solitons and S is the set of the (isolated) zeros of the analytic function *a(λ)* in $\mathbb{C}^+$ and $q(\lambda)$ is the continuous spectrum, which in general includes the whole real line, corresponds to the non-solitonic (or radiation) component of the signal (as shown in Fig. 4.2).

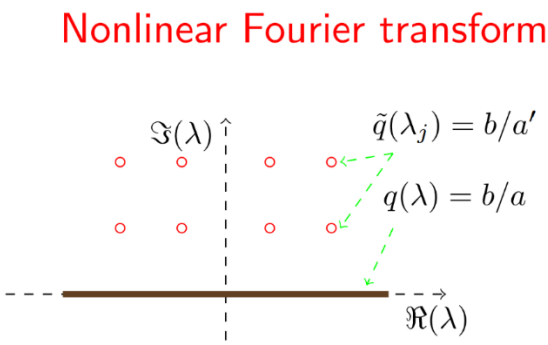

Fig. 4.2. The nonlinear spectrum of *q(t)*. Red dots in the upper half complex plane are its discrete part and the continuous part lays on the whole real line [42].

With the help of the NFT, a signal can be represented by its discrete and continuous nonlinear spectra. While the optical signal propagates along the fiber based on the complicated NLSE, the action of the channel on its spectral components obeying the evolution equation (3.4) will actually translate to the nonlinear Fourier coefficients as [42]

$$\begin{aligned} \hat{q}(z,\lambda) &= \hat{q}(0,\lambda) \cdot e^{-j4\lambda^2 z}, \\ \tilde{q}(z,\lambda_j) &= \tilde{q}(0,\lambda_j) \cdot e^{-j4\lambda^2 z}. \end{aligned} \tag{3.12}$$

Like the (ordinary) Fourier transform converting a linear convolutional channel $y(t) = x(t) * h(t)$ into a number of parallel scalar channels, the NFT converts a nonlinear dispersive channel described by NLSE into a number of parallel scalar channels having the "nonlinear transfer function"

$$H(\lambda) = e^{-j4\lambda^2 z} \tag{3.13}$$

4.3. Nonlinear Frequency Division Multiplexed Systems

Since the nonlinear Fourier spectrum $\hat{q}(0,\lambda),\tilde{q}(0,\lambda_j)$ does not interfere with each other upon transmissions in the nonlinear medium, this suggests that information can be encoded (in analogy with OFDM) in the nonlinear spectra. This scheme is referred to as nonlinear frequency division multiplexing (NFDM) [42].

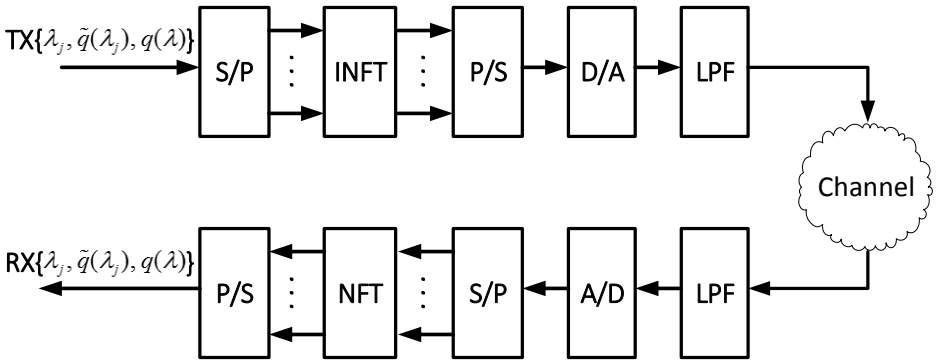

Fig. 4.3. The model of a NFDM system. [42].

Fig. 4.3 illustrates the scheme of a NFDM system which consists of two major steps. At first, the information is encoded in the nonlinear spectra of the signal at the transmitter side according to a suitable constellation on $\{\hat{q}(0,\lambda),\tilde{q}(0,\lambda_j)\}$. Each available degree of freedom on the discrete and/or continuous spectra can be modulated separately using OOK or QAM modulation. The time domain signal $q(t)$ is generated by taking the inverse nonlinear Fourier transform (INFT),

$$q(t,z) = INFT(\hat{q}(\lambda,z),\tilde{q}(\lambda_j,z)) \tag{3.14}$$

and then is launched into the channel. Several approaches can be taken to compute the INFT such as Riemann–Hilbert system of linear equations, Hirota bilinearization scheme and Darboux transformation [44], among which Darboux transformation is mainly used to generate multisoliton pulses and is particularly well suited for numerical implementation.

At the receiver side, the spectra (eigenvalues) of $q(t)$ are recovered by the (forward) NFT via,

$$\{\hat{q}(\lambda,z),\tilde{q}(\lambda_j,z)\} = NFT(q(t,z)) \tag{3.15}$$

and the resulting spectra are mapping back to the received information. Several algorithms can be used for NFT computation such as forward and central discretizations, fourth-order Runge-Kutta method, Layer-peeling method, Crank-Nicolson method and Ablowitz-Ladik algorithm [43].

In this OFDM-type NFDM scheme, although $q(t)$ is significantly distorted during propagation in the time domain and undergoes ISI in a very complicated manner based on the NLSE, the nonlinear spectra of the signal $\{\hat{q}(\lambda,z),\tilde{q}(\lambda_j,z)\}$ propagate independently of each other, and are held invariant during propagation, up to a complex-valued scale factor $e^{-j4\lambda^2 z}$ (as shown in Fig. 4.4). As a result, the ISI can be removed in the spectral domain and this transmission strategy is well suit for the nonlinear optical channel.

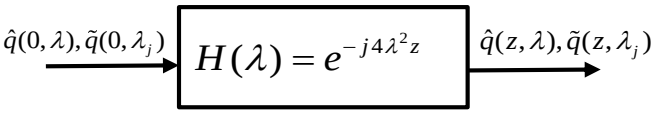

Fig. 4.4. The channel model of NFDM transmissions.

4.4. Experimental Demonstration of OOK Modulated NFDM Transmission

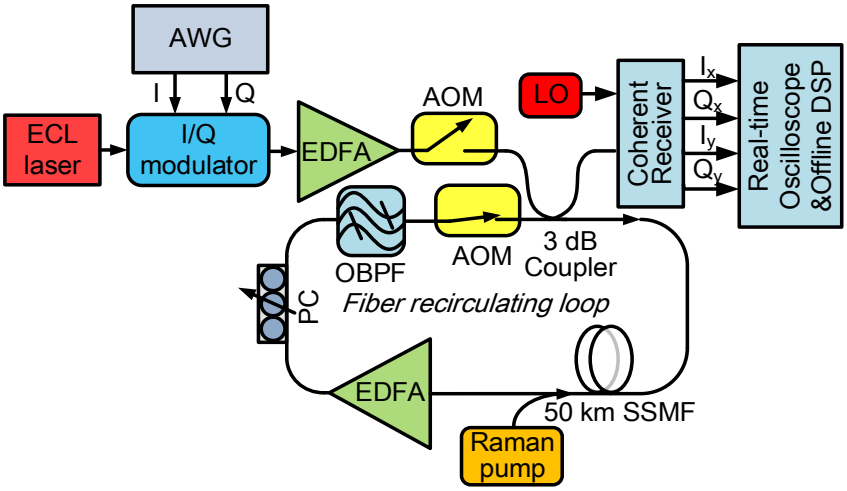

Fig. 4.5. Experimental setup for NFDM transmission. AWG: arbitrary waveform generator, AOM: acousto-optic modulator, OBPF: Optical band pass filter.

Fig. 4.5 shows the experimental setup for the OOK modulated NFDM transmission system, where we limit transmissions to signals with a small number of discrete eigenvalues, i.e., the support of the NFT

is in $\mathbb{C}^+$, with no continuous nonlinear spectral component. Jointly modulating N eigenvalues corresponds to N-soliton transmission. Starting from the trivial solution of NLS, the N-soliton signals are recursively computed using the Darboux transformation method [44]. These waveforms are then generated in the AWG and used to drive the IQ modulator. The output of the modulator is a train of optical soliton pulses, which are amplified and launched into a fiber recirculating loop. Since the theory of NFT is based on the integrability property of the lossless nonlinear Schrödinger equation, we use a short span of 50km SSMF and a distributed Raman amplifier in the recirculating loop to best approximate constant signal power evolution along the link. Note that we have applied the NFT to the normalized NLS equation. An EDFA is placed after the Raman amplifier to compensate the residual span loss and ensure the same launched power after each loop. A flat-top optical filter with a 3db bandwidth of 1nm is used inside the loop to suppress the out-of-band ASE noise. At the receiver, a polarization controller is used to align the signal in a particular polarization. The line-width of the transmitter and receiver lasers is 100 kHz. The transmitted signal is then coherently detected by an integrated coherent receiver and sampled by a digital storage scope with a sampling rate of 80GS/s and a bandwidth of 33GHz, which is followed by off-line digital signal processing.

4.4.1. 3-Eigenvalue Multi-soliton Transmission over 1800 km

For 3-eigenvalue NFDM signals, there are 7 different non-zero waveforms each corresponding to a distinct 3-bit sequence encoded in the 3 eigenvalues. The transmitted and received waveforms in our experiments are shown in Fig. 4.6(a). The average power and peak power of the waveform is 1.5 dBm and 12.3 dBm respectively and the overall bit rate is 1.5 Gbps. The first three pulses are 1-solitons of the form 2sech(2t), 4sech(4t) and 6sech(6t) that ideally retain their shape along transmission, while other pulses are different 2- and 3-solitons, corresponding to combinations of multiple eigenvalues. In general, the time-domain shapes of such higher-order solitons evolve with distance and are hence undesirable for traditional soliton communication systems with direct detection and minimal receiver DSP. However, with current digital coherent receivers, one can perform the NFT on the NFDM signals and, in the nonlinear frequency domain, the effect of the fiber will merely be a phase shift on the corresponding eigenvalues that do not interfere with each other along nonlinear fiber transmission.

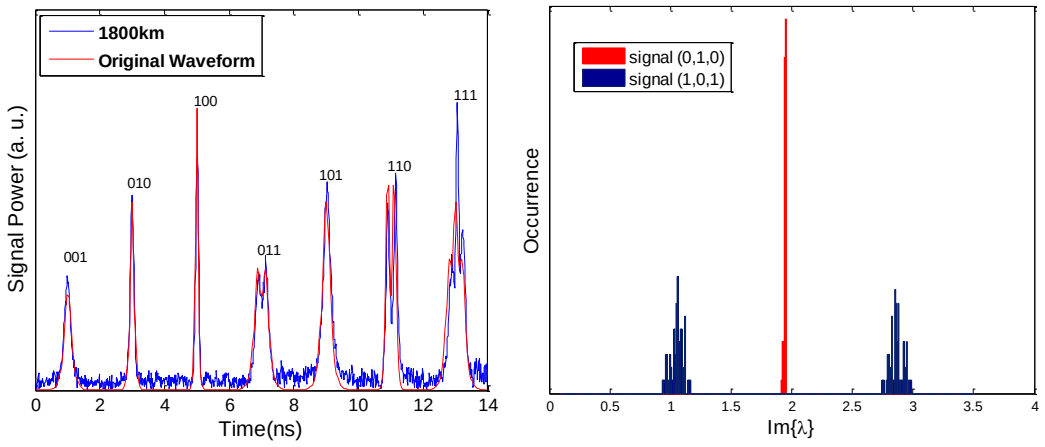

(a) (b)

Fig. 4.6 (a) Transmitted and received NFDM pulses for 7 different 3-eigenvalue NFDM signals over 1800 km; (b) Histogram plots of received eigenvalues for the NFDM signals (0,1,0) and (1,0,1).

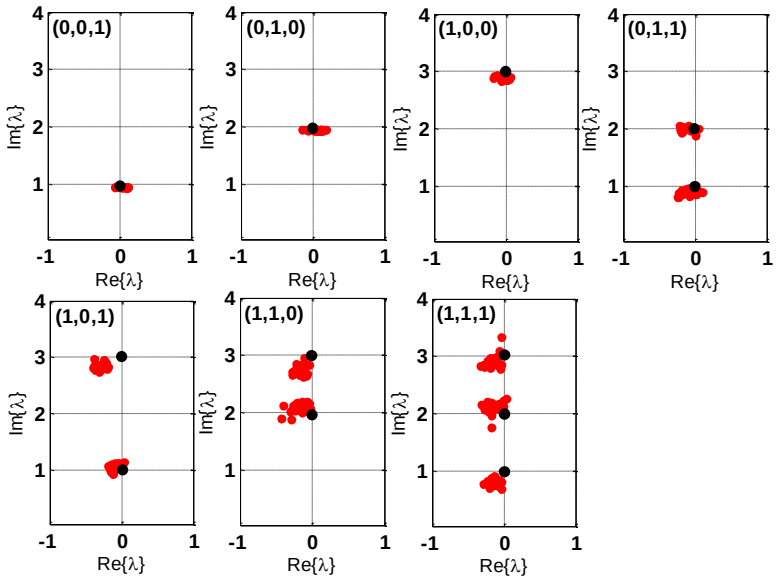

Fig. 4.7. Received eigenvalue distributions for 3-eigenvalue NFDM signals transmitted over 1800 km (black dots are ideal transmitted eigenvalues). The NFT of the signal (0,0,0) is not shown.

Frequency-offset compensation was first applied to the received signal. Since our multi-soliton NFDM signals are constituted by independent intensity modulation of multiple eigenvalues, carrier phase estimation is not necessary for symbol detection after receiver NFT. In general when information is encoded in both the phase and amplitude of the eigenvalues, however, carrier phase estimation will be much needed and this is a good and important topic for future research. The received-signal samples

were then interpolated, normalized and put into the NFT computation consisting of Ablowitz-Ladik algorithm followed by Newton Raphson method to obtain the eigenvalues [43]. The distributions of the received eigenvalues are shown in Fig. 4.7 for different NFDM signals and the histogram plots of the received eigenvalues for the NFDM signals (0,1,0) and (1,0,1) are shown in Fig. 4.6(b). We can observe that the eigenvalues are clearly received and distinguishable even after 1800 km propagation in the fiber links, which indicates error-free transmissions. It should be noted that in this experiment, we are only modulating the location (imaginary part) of the eigenvalues in the upper-half complex plane. The overall data-rate can be considerably improved by also modulating other degrees of freedom of the NFT spectrum, including the continuous spectrum [74], the real part and/or the phase of the eigenvalues [70][75].

4.4.2. 4-Eigenvalue Multi-soliton Transmission over 200 km

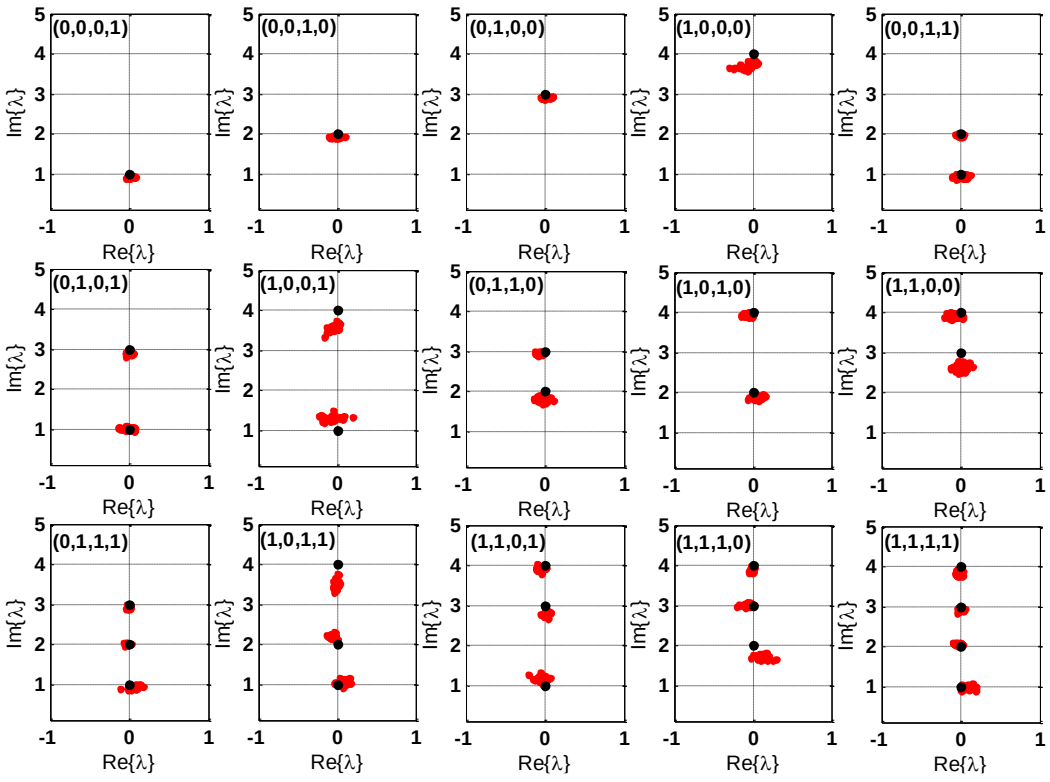

Fig. 4.8. Received eigenvalue distributions for 4-eigenvalue NFDM signals transmitted over 200 km. (Black dots are ideal transmitted eigenvalues). The NFT of the signal (0,0,0,0) is not shown.

We also attempted the transmission of 4-eigenvalue NFDM signals and Fig. 4.8 shows the

received eigenvalue distributions for the 15 distinct non-zero NFDM signals after 200 km of error-free transmission. NFDM with 4 eigenvalues is more sensitive to hardware imperfections and system parameters such as Raman pump power and transmit signal power. Nevertheless, it is expected that more detailed NFDM experiments will lead to better transmission performance in the future.

4.5. Impact of Frequency Offset and Laser Phase Noise on OOK modulated NFDM Systems

We also study the impact of frequency offset and laser phase noise on the OOK modulated NFDM systems. The simulation setup is the same as that used for experiments which is shown in Fig. 4.5. Let $q(t) \leftrightarrow (\hat{q}(\lambda), \tilde{q}(\lambda_j))$ be a nonlinear Fourier transform pair, where $\hat{q}(\lambda)$ and $\tilde{q}(\lambda_j)$ denote its continuous and discrete nonlinear spectra, respectively, and according to the frequency shift and phase change properties of the NFT [42],

$$q(t)e^{-2j\omega t} \leftrightarrow (\hat{q}(\lambda-\omega), \tilde{q}(\lambda_k-\omega)) \tag{3.16}$$

$$e^{j\phi}q(t) \leftrightarrow e^{-j\phi}(\hat{q}(\lambda), \tilde{q}(\lambda_k)), \tag{3.17}$$

the frequency offset ω between transmitter and receiver will just introduce a real-part shift of the received eigenvalue and a constant phase rotation ϕ in time domain will introduce negative phase rotation to the received nonlinear spectra.

Simulations are performed where the frequency offset between transmitter and receiver is set to -1.5 GHz to +1.5 GHz with a step of 500 MHz and the laser linewidth of both transmitter and receiver is set to 100k, 1M and 10M Hz. Fig. 4.9 shows the distributions of the received eigenvalues for the NFDM signals (1,1,1) of back to back transmission and over 1200 km propagation in the presence of different frequency offset when the laser linewidth is set to be 0. We can observe that all the eigenvalues are clearly received and distinguishable for both cases. The eigenvalues shift horizontally from left to the right in the upper half complex plane $\mathbb{C}^+$ as the frequency offset changes from -1.5 GHz to +1.5 GHz. The distributions of eigenvalues for other NFDM signal present a same trend and will be omitted here. It proves that the frequency offset will only shift the real-part of the received eigenvalue and it will not degrade the performance of OOK NFDM system since the symbol decision only utilize the image part of eigenvalues. In fact, in NFT philosophy the real-part of eigenvalue equals to the frequency ω in the frequency domain of tradition Fourier transform. In other word, it provides us another degree of freedom to modulate the real part of the eigenvalues in the upper-half complex plane that can further improve the overall data-rate of NFDM communication. Noted that in Fig. 4.9(b) due to the non-

lossless transmission the image part of eigenvalues after 1200 km propagation are little bit away from their original location.

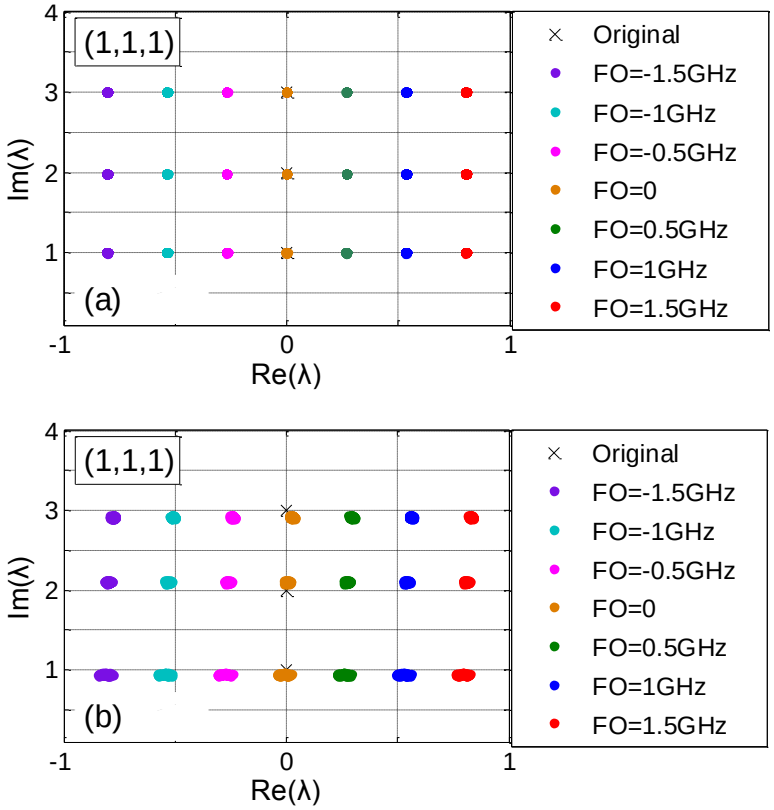

Fig. 4.9. Distributions of the received eigenvalues for the NFDM signals (1,1,1) of back to back transmission (a) and over 1200 km propagation (b) in the presence of different frequency offset.

Fig. 4.10 shows the distributions of the received eigenvalues for the NFDM signals (1,0,0), (1,1,0) and (1,1,1) of both back to back transmission and over 1200 km propagation of different laser linewidth when the frequency offset is set to be 0. As shown in Fig. 4.10(a), only the real part of eigenvalues spreads as the laser width increases in the back to back scheme. When propagating in the fiber links, the eigenvalue-distribution of NFDM signals (1,1,0) and (1,1,1) that are composed of multi-eigenvalue and have deep V and multi-peak pulse shape will spreads both along real and imaginary axis, whereas the eigenvalue-distribution of NFDM signals (1,0,0) composed of single-eigenvalue and has sech pulse shape only spreads along real axis. As the laser linewidth increases, the distribution of multi-soliton will further spread along both axis, which is deemd due to the nonlinear interaction between signal and noise. However, in practical system, where the typical laser linewidth is several hundred KHz, the

impact of laser phase noise on OOK NFDM systems can be neglected as there is only slight spreading when the laser linewidth increases from 100 kHz to 1 MHz.

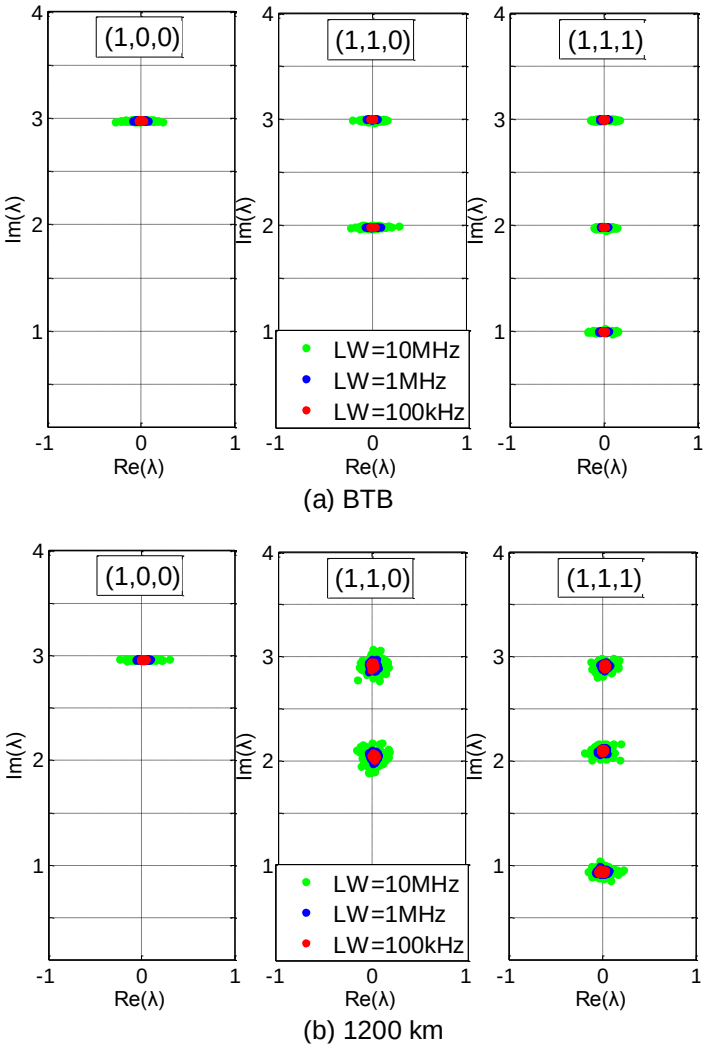

Fig. 4.10. Distributions of the received eigenvalues for the NFDM signals(1,0,0), (1,1,0) and (1,1,1) of back to back transmission (a) and over 1200 km propagation (b) of different laser linewidth.

4.6. Summary

In this chapter, we experimentally demonstrate for the first time the successful modulation and detection of 3-eigenvalue OOK modulated NFDM signals over 1800 km based on the recently proposed NFT framework. Extensions to 4-eigenvalue transmissions are also experimentally investigated. We also studied the impact of frequency offset and laser phase noise on such systems and the results showed that they are robust to the frequency offset and laser phase noise in a certain range. We believe that

much more remains to be investigated in deriving practical and comprehensive NFT-based communication strategies that fully embrace fiber nonlinearity. NFDM signaling appears to hold much promise as a nonlinearity-compatible fiber-optic transmission technology.

Chapter 5

Conclusion and Future Outlook

As today's optical communication systems has evolved to the digital coherent systems where the accumulated ASE noise and nonlinearity are the fundamental capacity-limiting factors, this thesis focus on the development of OSNR monitoring techniques and transmission strategies for long-haul coherent systems.

In Chapter 2, a fiber-nonlinearity-insensitive OSNR monitoring technique is proposed. It characterize the fiber nonlinearity induced amplitude noise correlation among neighboring symbols as a quantitative measure of nonlinear distortions to the signal. Therefore nonlinear-insensitivity is achieved by calibrating such amplitude noise correlations into the EVM-based OSNR estimator. However, it may not work properly in the presence of inter-channel nonlinearities since only amplitude noise correlation among neighboring symbols are taken into consideration as the quantitative measure of nonlinear distortions. Further investigations on the proposed methodology to estimate the OSNR accurately without the prior knowledge of the system configurations such as the transmission distance and number of WDM channels will be attempted in the future. This can result in a nonlinearity-insensitive OSNR monitoring technique that is applicable in dynamic and flexible network environments, which may hold key to its commercial implementation in software defined networks.

In Chapter 3, a low-cost and filtering-effect-insensitive OSNR monitor for distributed monitoring of optical networks is studied which utilizes reduced-complexity coherent receptions, electrical filtering and RF power measurements. By measuring the RF power of three different frequency components of the coherently received baseband signals, the proposed technique is insensitive to spectral narrowing by WSSs. However, it can not work for the Nyquist pulse shape where the signal spectrum is flat on the three different frequencies. It also would be unrealistic for such technique working without any prior knowledge of the pulse shape and WSS shape. Hence in the future, data-aided OSNR monitoring technique may be needed for inline cost-effective OSNR monitoring.

In Chapter 4, motivated by the fact that optical coherent systems are severely limited by the impacts of the nonlinearity, we present the framework of NFDM systems which is fundamentally compatible with the structure of the nonlinear channel. As the signal power or transmission distance is

increased, the newly proposed method does not suffer from the cross talk between signal components, which has limited the performance of the prior work. We took the first steps towards a NFDM communication system implementing the nonlinear Fourier transform, where the transmission of multi-eigenvalue OOK NFDM signals over 1800 km is experimental demonstrated for the first time. The robustness of such system to the frequency offset and laser phase noise is also investigated. Naturally, the next step from a communication theory standpoint is phase modulation on the eigenvalues as this is a new degree of freedom to encode information compared with traditional soliton research and will be a key component in NFDM transmissions. Furthermore, NFDM systems utilizing high modulation format such as QAM simultaneously both on the discrete and continuous spectrum should ultimately be achieved in the future to fully exploit the degree of freedom on the nonlinear spectrum and explore all the available capacity.

Reference

[1] G. P. Agrawal, Nonlinear Fiber Optics. Academic Press (3. Edition, 2001)

[2] S. J. Savory, “Digital coherent optical receivers: algorithms and subsystems,” IEEE J. Sel. Top. Quantum Electron. 16(5), 1164–1179 (2010).

[3] A. Galtarossa and C. R. Menyuk, Eds., Polarization Mode Dispersion. New York: Springer, 2005.

[4] G. P. Agrawal, Lightwave Technology: Telecommunication Systems. New York: Wiley, 2005.

[5] R.-J. Essiambre, G. Kramer, P.J. Winzer, G.J. Foschini and B. Goebel, “Capacity limits of optical fiber networks”, IEEE J. Lightw.Technol, vol. 28, pp. 662-701, 2010.

[6] E. F. Mateo, F. Yaman, and G. Li, “Efficient compensation of interchannel nonlinear effects via digital backward propagation in WDM optical transmission,” Opt. Express, vol. 18, no. 14, pp. 15144–15154, 2010.

[7] K. Kikuchi, “Digital coherent optical communication systems: Fundamentals and future prospects,” IEICE Electron. Exp., vol.8, no.20,pp.1642-1662, Oct. 2011.

[8] Z. Jia, et al. "Dual-carrier 400G solutions based on 8/16/32-QAM modulation formats," Photonics Conference (IPC), 2015. IEEE, 2015.

[9] J. Lai, et al. "Evaluation of key parameters of 400Gbps WDM system," Optoelectronics Global Conference (OGC), 2015. IEEE, 2015.

[10] F. Zhang, et al. "Terabit Coherent Optical Transmission of Nyquist PDM 64-QAM Signal," Optoelectronic Devices and Integration. Optical Society of America, 2015.

[11] F.N. Khan, T.S.R. Shen, Y. Zhou, A.P.T. Lau and C. Lu, “Optical performance monitoring using artificial neural networks trained with empirical moments of asynchronously sampled signal amplitudes,” IEEE Photonics Technology Letters, vol. 24, no. 12, June 2012.

[12] J. H. Lee, D. K. Jung, C. H. Kim, and Y. C. Chung, “OSNR monitoring technique using polarization nulling method,” IEEE Photonics Technology Letters, vol. 13, no. 1, pp. 88–90, 2001.

[13] Q Sui, A. P. T. Lau and C. Lu, “OSNR monitoring in the presence of first order PMD using polarization diversity and DSP,” IEEE/OSA Journal of Lightwave Technology, vol. 28, no. 15, pp. 2105–2114, (2010).

[14] S. L. Woodward, L. E. Nelson, M. D. Feuer, X. Zhou, P. D. Magill, S. Foo, D. Hanson, H. Sun, M. Moyer, and M. O'Sullivan, "Characterization of real-Time PMD and chromatic dispersion monitoring in a high-PMD 46-Gb/s transmission system," IEEE Photonics Technology Letters, vol. 20, no. 24, pp. 2048–2050, 2008.

[15] J. C. Geyer, C. R. S. Fludger, T. Duthel, C. Schulien, and B. Schmauss,"Performance monitoring using coherent receivers," in Proc. Optical Fiber Communication Conference, Feb. 2009, Paper OThH5.

[16] F. N. Hauske, M. Kuschnerov, B. Spinnler, and B. Lankl, "Optical performance monitoring in digital coherent receivers," IEEE/OSA Journal of Lightwave Technology, vol. 27, no. 16, 3623-3631(2009).

[17] Q. Yu, Z. Pan, L.-S. Yan and A.E. Willner, "Chromatic dispersion monitoring technique using sideband optical filtering and clock phase-shift detection," IEEE/OSA Journal of Lightwave Technology, vol. 20, no. 12, pp. 2267–2271, Dec. 2002.

[18] Z. Pan, Y. Xie, S.A. Havstad, Q. Yu, A.E. Willner, V. Grubsky, D.S. Starodubov and J. Feinberg, "Real-time group-velocity dispersion monitoring and automated compensation without modifications of the transmitter," Optics Communications, 230(1–3), pp. 145–149, 2004.

[19] Y.K. Lize′, L. Christen, J.-Y. Yang, P. Saghari, S. Nuccio, A.E. Willner and R. Kashyap, "Independent and simultaneous monitoring of chromatic and polarization-mode dispersion in OOK and DPSK transmission," IEEE Photonics Technology Letters, vol. 19, no. 1, pp. 3–5, Jan. 2007.

[20] Y. Wang, S. Hu, L. Yan, J.-Y. Yang and A.E. Willner, "Chromatic dispersion and polarization mode dispersion monitoring for multi-level intensity and phase modulation systems," Optics Express, vol. 15, no. 21, pp. 14038–14043, Oct. 2007.

[21] G. Rossi, T.E. Dimmick and D.J. Blumenthal, "Optical performance monitoring in reconfigurable WDM optical networks using subcarrier multiplexing," IEEE/OSA Journal of Lightwave Technology, vol. 18, no. 12, pp. 1639–1648, Dec. 2000.

[22] M.N. Petersen, Z. Pan, S. Lee, S.A. Havstad and A.E. Willner, “Online chromatic dispersion monitoring and compensation using a single inband subcarrier tone,” IEEE Photonics Technology Letters, vol. 14, no. 4, pp. 570–572, Aug. 2002.

[23] A. Liu, G.J. Pendock and R.S. Tucker, “Improved chromatic dispersion monitoring using single RF monitoring tone,” Optics Express, vol. 14, no. 11, pp. 4611–4616, May 2006.

[24] H. C. Ji, K. J. Park, J. H. Lee, H. S. Chung, E. S. Son, K. H. Han, S. B. Jun, and Y. C. Chung, “Optical performance monitoring based on pilot tones for WDM network applications,” Journal of Optical Networking, vol. 4, no. 7, pp. 510 533, Jul. 2004.

[25] E. Ip, A. P. T. Lau, D. J. F. Barros, and J. M. Kahn, “Coherent detection in optical fiber systems,” Optics Express, vol. 16, no. 2, pp. 753–791, Jan. 2008.

[26] X. Liu, Y. H. Kao, S. Chandrasekhar, I. Kang, S. Cabot, and L. L. Buhl, “OSNR monitoring method for OOK and DPSK based on optical delay interferometer,” IEEE Photonics Technology Letters, vol. 19, no. 15, pp. 1172–1174, 2007.

[27] D.J. Ives, B.C. Thomsen, R. Maher, and S. Savory, “Estimating OSNR of equalised QPSK signals,” in Proc. European Conference and Exhibition on Optical Communication (ECOC), 2011, Paper Tu.6.A.6.

[28] M. S. Faruk and K. Kikuchi, “Monitoring of optical signal-to-noise ratio using statistical moments of adaptive-equalizer output in coherent optical receivers,” in Proc. Opto-Electronics and Communications Conference(OECC), pp. 233–234, 2011.

[29] M. S. Faruk, Y. Mori and K. Kikuchi, “In-Band estimation of optical signal-to-noise ratio from equalized signals in digital coherent receivers,” IEEE Photonics Journals, vol. 6, no. 1, Feb. 2014.

[30] C. Zhu, A. V. Tran, S. Chen, L. Du, C. Do, T. Anderson, A. Lowery, and E. Skafidas, “Statistical moments-based OSNR monitoring for coherent optical systems,” Optics Express, vol. 20, no. 16, pp. 17711–17721, Jul. 2012.

[31] C. Do, A. V. Tran, C. Zhu, D. Hewitt, and E. Skafidas, “Data-Aided OSNR estimation for QPSK and 16-QAM coherent optical system,” IEEE Photonics Journals, vol. 5, no. 5, Oct. 2013.

[32] F. Pittalà, F. N. Hauske, Y. Ye, N. G. Gonzalez, and I. T. Monroy, “Joint PDL and in-band OSNR monitoring supported by data-aided channel estimation,” in Proc. Optical Fiber Communication Conference, Mar. 2012, Paper OW4G.

[33] E. Ip, “Nonlinear compensation using backpropagation for polarization-multiplexed transmission,” IEEE J. Lightwave Technol. 28(6), 939–951 (2010).

[34] R.-J. Essiambre, G. Kramer, P.J. Winzer, G.J. Foschini and B. Goebel, “Capacity limits of optical fiber networks”, IEEE J. Lightw.Technol, vol. 28, pp. 662-701, 2010.

[35] D. Rafique, T. Rahman, A. Napoli, and B. Spinnler, “Digital Pre Emphasis in Optical Communication Systems: On the Nonlinear Performance,” J. Light. Technol., vol. 33, no. 01, pp. 140–150, Jan. 2015.

[36] M. Morshed, A. J. Lowery, and L. B. Du, “Improving performance of optical phase conjugation by splitting the nonlinear element,” Opt. Express, vol. 21, no. 4, pp. 4567–77, Feb. 2013.

[37] E. Ip and J. Kahn, “Compensation of Dispersion and Nonlinear Effects using Digital Backpropagation”, IEEE J. Lightw.Technol, vol. 26, no. 20, pp. 3416–3425, Oct. 2008.

[38] D. Rafique, J. Zhao, and A. D. Ellis, “Performance improvement by fibre nonlinearity compensation in 112 Gb/s PM M-ary QAM,” Opt. Fiber Commun. Conf., 2011, OWO6.

[39] E. F. Mateo, F. Yaman, and G. Li, “Efficient compensation of interchannel nonlinear effects via digital backward propagation in WDM optical transmission,” Opt. Express, vol. 18, no. 14, pp. 15144–15154, 2010.

[40] G. Liga, T. Xu, A. Alvarado, R. I. Killey, and P. Bayvel, “On the performance of multichannel digital backpropagation in high-capacity long-haul optical transmission,” Opt. Express, vol. 22, no. 24, 30053–30062, 2014.

[41] D. Rafique, "Fiber Nonlinearity Compensation: Commercial Applications and Complexity Analysis," in Lightwave Technology Journal, vol.PP, no.99, pp.1-1, 2015.

[42] M. I. Yousefi and F. R. Kschischang, “Information Transmission using the Nonlinear Fourier Transform, Part I: Mathematical Tools”, IEEE Trans. Inf. Theory, vol. 60, no. 7, pp. 4312–4328, Jul. 2014.

[43] M. I. Yousefi and F. R. Kschischang, “Information Transmission using the Nonlinear Fourier Transform, Part II: Numerical Methods”, IEEE Trans. Inf. Theory, vol. 60, no. 7, pp. 4329–4345, Jul. 2014.

[44] M. I. Yousefi and F. R. Kschischang, “Information Transmission using the Nonlinear Fourier Transform, Part III: Spectrum Modulation,” IEEE Trans. Inf. Theory, vol. 60, no. 7, pp. 4346–4369, Jul. 2014.

[45] D. C. Kilper, S. Chandrasekhar, L. Buhl, A. Agarwal, and D. Maywar, “Spectral monitoring of OSNR in high speed networks,” in European Conference and Exhibition on Optical Communication (ECOC), 2002, paper 7.4.4.

[46] S. D. Dods and T. B. Anderson, “Optical Performance Monitoring Technique Using Delay Tap Asynchronous Waveform Sampling,” in Proc. OFC’06 , Anaheim, California, Mar. 2006, Paper OThP5.

[47] J. Jargon, X. Wu, and A. E. Willner, “Optical performance monitoring using artificial neural networks trained with eye-diagram parameters,” IEEE Photon. Technol. Lett. 21(1), 54–56 (2009).

[48] R. Schmogrow, B. Nebendahl, M. Winter, A. Josten, D. Hillerkuss, S. Koenig, J. Meyer, M. Dreschmann, M. Huebner, C. Koos, J. Becker, W. Freude, and J. Leuthold, “Error Vector Magnitude as a Performance Measure for Advanced Modulation Formats,” IEEE Photon. Technol. Lett. 24(1), 61–63 (2012).

[49] M. Mayrock and H. Haunstein, “Optical monitoring for non-linearity identification in CO-OFDM transmission systems,” in Proc. OFC’08, San Diego, CA, Feb. 2008, Paper JThA58.

[50] J. Renaudier, G. Charlet, O. Bertran-Pardo, H. Mardoyan, P. Tran, M. Salsi, and S. Bigo, “Transmission of 100Gb/s Coherent PDM-QPSK over 16x100km of Standard Fiber with all-erbium amplifiers,” Optics Express. 17(7), 5112–5117 (2009).

[51] A. H. Gnauck, P. J. Winzer, S. Chandrasekhar, X. Liu, B. Zhu, and D. W. Peckham, “Spectrally Efficient Long-Haul WDM Transmission Using 224-Gb/s Polarization-Multiplexed 16-QAM,” J. Lightwave. Technol. 29(4), 373–377 (2011).

[52] P. Poggiolini, A. Carena, V. Curri, G. Bosco, and F. Forghieri, "Analytical Modeling of Nonlinear Propagation in Uncompensated Optical Transmission Links," IEEE Photon. Technol. Lett. 23(11), 742–744 (2011).

[53] F. Vacondio, O. Rival, C. Simonneau, E. Grellier, A. Bononi, L. Lorcy, J. C. Antona, and S. Bigo "On nonlinear distortions of highly dispersive optical coherent systems," Optics Express, 20(2), 1022–1032 (2012).

[54] A. Bononi, P. Serena, N. Rossi, and D. Sperti, "Which is the Dominant Nonlinearity in Long-haul PDM-QPSK Coherent Transmissions?" in European Conference and Exhibition on Optical Communication (ECOC), 2010, Th.10.E.1.

[55] A. Bononi, N. Rossi, and P. Serena, "Transmission Limitations due to Fiber Nonlinearity," in Proc. OFC'11 , Los Angeles, Mar. 2011, Paper OWO7.

[56] A. P. T. Lau, S. Rabbani, and J. M. Kahn, "On the statistics of intra-channel four-wave mixing in phase-modulated optical communication systems," J. Lightwave. Technol. 26(14), 2128–2135 (2008).

[57] Optical Monitoring for DWDM Systems. ITU-T recommendation G.697, June 2004.

[58] VPIsystemsTM, "VPltransmissionMakerTM".

[59] X. Zhou, J. Yu, and P. D. Magill, "Cascaded two-modulus algorithm for blind polarization de-multiplexing of 114-Gb/s PDM-8-QAM optical signals," in Proc. OFC'09, San Diego, Mar. 2009, Paper OWG3.

[60] Y. L. Gao, A.P.T. Lau, S. Y. Yan, and C. Lu, "Low-complexity and phase noise tolerant carrier phase estimation for dual-polarization 16-QAM systems," Optics Express. 19(22), 21717-21729 (2011).

[61] O. Vassilieva, T. Hoshida, X. Wang, J. Rasmussen, H. Miyata, and T. Naito, "Impact of Polarization Dependent Loss and Cross-Phase Modulation on Polarization Multiplexed DQPSK Signals," in Proc. OFC'08, San Diego, CA, Feb. 2008, Paper OThU6

[62] A. P. T. Lau, Y. Gao, Q. Sui, D. Wang, Q. Zhuge, M. Morsy-Osman, M. Chagnon, X. Xu, C. Lu, and D. V. Plant, "Advanced DSP techniques enabling high spectral efficiency and flexible transmissions: toward elastic optical networks," IEEE Signal Process. Mag. 31(2), 82–92 (2014).

[63] X. Liu, Y. H. Kao, S. Chandrasekhar, I. Kang, S. Cabot, and L. L. Buhl, “OSNR monitoring method for OOK and DPSK based on optical delay interferometer,” IEEE Photon. Technol. Lett. 19(15), 1172–1174 (2007).

[64] S. Oda, J. Y. Yang, Y. Akasaka, K. Sone, Y. Aoki, M. Sekiya, and J. C. Rasmussen, “In-band OSNR monitor using an optical bandpass filter and optical power measurements for superchannel signals,” in Proc. Eur. Conf. Exhib. Opt. Commun. (ECOC), London, U. K., Sep. 2013, paper P.3.12.

[65] G. Nakagawa, S. Oda, K. Sone, Y. Aoki, T. Hoshida, and J. C. Rasmussen, “Demonstration of integrated optical path monitoring sub-system in CDCG-ROADM network,” in Proc. Eur. Conf. Exhib. Opt. Commun. (ECOC), Cannes, France, Sep. 2014, paper P.4.1.

[66] C. Pulikkaseril, L. A. Stewart, M. A. Roelens, G. W. Baxter, S. Poole, and S. Frisken, “Spectral modeling of channel band shapes in wavelength selective switches,” Opt. Express 19(9), 8458–8470 (2011).

[67] H. Rosenfeldt, I. Clarke, S. Frisken, G. Dash, X. Huang, H. Li, W. Cui, J. Zhang, J. Chen, Z. Kong, and S. Poole, “Miniaturized heterodyne channel monitor with tone detection,” in Proc. Opt. Fiber Commun. (OFC), Los Angeles, CA, Mar. 2015, Paper W4D.7.

[68] Y. Sakamaki, T. Kawai, T. Komukai, M. Fukutoku, and T. Kataoka, “Evaluation of optical filtering penalty in digital coherent detection system,” in IEICE Commun. Express, 1(2), 54-59 (2012).

[69] R.-J. Essiambre, G. Kramer, P.J. Winzer, G.J. Foschini and B. Goebel, “Capacity limits of optical fiber networks”, IEEE J. Lightw.Technol, vol. 28, pp. 662-701, 2010.

[70] H. Bülow, “Experimental Demonstration of Optical Signal Detection Using Nonlinear Fourier Transform," IEEE J. Lightw.Technol, vol. 33, no. 7, pp. 1433–1439, Apr. 2015.

[71] H. Terauchi and A. Maruta, “Eigenvalue Modulated Optical Transmission System Based on Digital Coherent Technology,” paper WR2-5, OECC 2013,

[72] Y. Matsuda, H. Terauchi and A. Maruta, “Design of Eigenvalue-multiplexed Multi-level Modulation Optical Transmission System”, pp. 1016-1018, OECC/ACOFT2014.

[73] H. Terauchi, Y. Matsuda, A. Toyota and A. Maruta, “Noise Tolerance of Eigenvalue Modulated Optical Transmission System Based on Digital Coherent Technology,” pp. 778-780, OECC/ACOFT 2014.

[74] S. T. Le, J.E. Prilepsky and S. K. Turitsyn, “Nonlinear Inverse Synthesis Technique for Optical Links with Lumped Amplification”, Opt.Express, vol. 23, no. 7, pp. 8317–8328, Apr. 2015.

[75] V. Aref, H. Büow, K. Schuh and W. Idler, “Experimental Demonstration of Nonlinear Frequency DivisionMultiplexed Transmission,” in Proc. ECOC 2015, paper Tu 1.1.2.

[76] P. D. Lax, “Integrals of nonlinear equations of evolution and solitary waves,” Comm.Pure Appl. Math, vol. 21, no. 5, pp. 467–490, 1968.

[77] M. J. Ablowitz, D. J. Kaup, A. C. Newell, and H. Segur, “The inverse scattering transform Fourier analysis for nonlinear problems,” *Stud. Appl. Math.*, vol. 53, pp.249–315, 1974.